Prepared for submission to JINST

Recent Advances in Combined Positron Emission Tomography and Magnetic Resonance Imaging

P. Galve,[a] **B. Rodriguez-Vila,**[b] **J.L. Herraiz,**[a] **V. García-Vázquez,**[b] **N. Malpica,**[b] **J.M. Udias**[a] **and A. Torrado-Carvajal,** [b,1]

[a] *Nuclear Physics Group and IPARCOS, Faculty of Physical Science, Universidad Complutense de Madrid, Madrid, Spain*

[b] *Medical Image Analysis and Biometry Lab, Universidad Rey Juan Carlos, Móstoles, Spain*

E-mail: angel.torrado@urjc.es

Abstract: Hybrid imaging modalities combine two or more medical imaging techniques offering exciting new possibilities to image the structure, function and biochemistry of the human body in far greater detail than has previously been possible to improve patient diagnosis. In this context, simultaneous Positron Emission Tomography and Magnetic Resonance (PET/MR) imaging offers great complementary information, but it also poses challenges from the point of view of hardware and software compatibility. The PET signal may interfere with the MR magnetic field and vice-versa, posing several challenges and constrains in the PET instrumentation for PET/MR systems. Additionally, anatomical maps are needed to properly apply attenuation and scatter corrections to the resulting reconstructed PET images, as well motion estimates to minimize the effects of movement throughout the acquisition. In this review, we summarize the instrumentation implemented in modern PET scanners to overcome these limitations, describing the historical development of hybrid PET/MR scanners. We pay special attention to the methods used in PET to achieve attenuation, scatter and motion correction when it is combined with MR, and how both imaging modalities may be combined in PET image reconstruction algorithms.

Keywords: Hybrid Imaging, Medical Imaging, Multi-Modality Systems, PET, MR

[1]Corresponding author.

Contents

1 Introduction

Diagnostic and research medical imaging are intrinsically multimodal. Each modality offers specific structural or functional information about the anatomical region being studied and/or treated, and this information is associated with potential disease, injury, or the efficacy of a therapy. For example, Computerized Tomography (CT) quantifies electron density, Positron Emission Tomography (PET) determines concentration and distribution of a radiotracer in the patient, while Magnetic Resonance (MR) imaging displays proton density and magnetic properties [1].

Imaging modalities have been evolving to constantly adapt to changing needs. New scanners have benefited from technological advancements increasing their acquisition speed, spatial resolution, and image contrast. They now produce better images that allow physicians to better diagnose diseases and carry out medical procedures with greater confidence. At the same time, medical imaging researchers have worked on improving and combining the various equipment to obtain complementary information or address the limitations of each of the imaging modalities. Obtaining

multimodal images is not straightforward. Moving the patient from one scanner to another in a clinical setting is not easy and, depending on the position of the patient in the different scanners, the acquired images could present a different spatial distortion. Thus, the need for precisely aligned anatomical and functional imaging led to the development of the hybrid PET/CT scanner [2]. PET/CT scanners soon became widespread clinical equipment [3], while the development of combined PET/MR scanners took longer because of various technical challenges of both technologies [4, 5]. Although the combination of PET and MR was already mentioned in a PhD thesis in 1991 [6], and simultaneous PET/MR acquisition was demonstrated in 1997 [7], it took an additional 13 years for clinical systems to be commercially available [8].

Currently, several studies are demonstrating the benefits of hybrid PET/MR imaging compared to PET/CT, including simultaneous acquisition to accurately quantify tissue and/or organ functionality from complementary modalities, reduced exposure to radiation and contrast-enhanced soft tissue [9–18]. These benefits are the result of truly simultaneous data acquisition avoiding the need for patient-specific CT images -and thus reducing the ionizing radiation dose- and the MR superior soft tissue contrast allowing for better anatomical localization of activity in PET.

However, these new hybrid PET/MR scanners also come with new practical limitations for clinical application compared to equivalent PET/CT systems, e.g., increased noise, different artifacts, attenuation correction (AC) issues, and new safety concerns. Moreover, implementing both technologies in the same bore is challenging, as they caused interference with one another, compromising the final image quality.

2 PET instrumentation for PET/MR systems

The typical detectors used in PET have been adopted from traditional nuclear physics to optimize gamma photons detection with high sensitivity, fast response, high spatial resolution, and reasonable energy resolution [19]. Good efficiency is needed to obtain an equivalent image signal-to-noise ratio (SNR) with a reduced delivered dose to the patient. The total efficiency is a combination of geometry (solid angle of the patient covered by the scanner) and detector intrinsic efficiency. Nowadays, total-body scanners up to 1 or 2 m long have been introduced in order to increase scanner efficiency [20]. High temporal resolution with a narrower coincidence time window aids to reduce random coincidences (figure 1). Furthermore, below 1 ns, the coincidence time resolution (CRT) enables the use of time-of-flight (TOF) information to reduce the uncertainty in the coincidence positioning (figure 2), increasing the effective efficiency [21–23]. Equivalently, it is interesting to precisely locate the interaction point of the photon within the detector to define narrower lines of response (LORs) and reduce the depth of interaction uncertainty (DOI, figure 1), increasing image resolution. Energy resolution allows distinguishing 511 keV photons from scattered photons (figure 1), which may achieve up to 50% of the coincidences in clinical scenarios [24, 25].

The strong magnetic fields used in MR, of the order of a few Tesla, may interfere with PET detectors distorting the PET signal. In this section, we focus on the main components of the PET detector and their compatibility with MR scanners:

- The scintillator crystal absorbs the gamma radiation and transforms it into a secondary light signal.

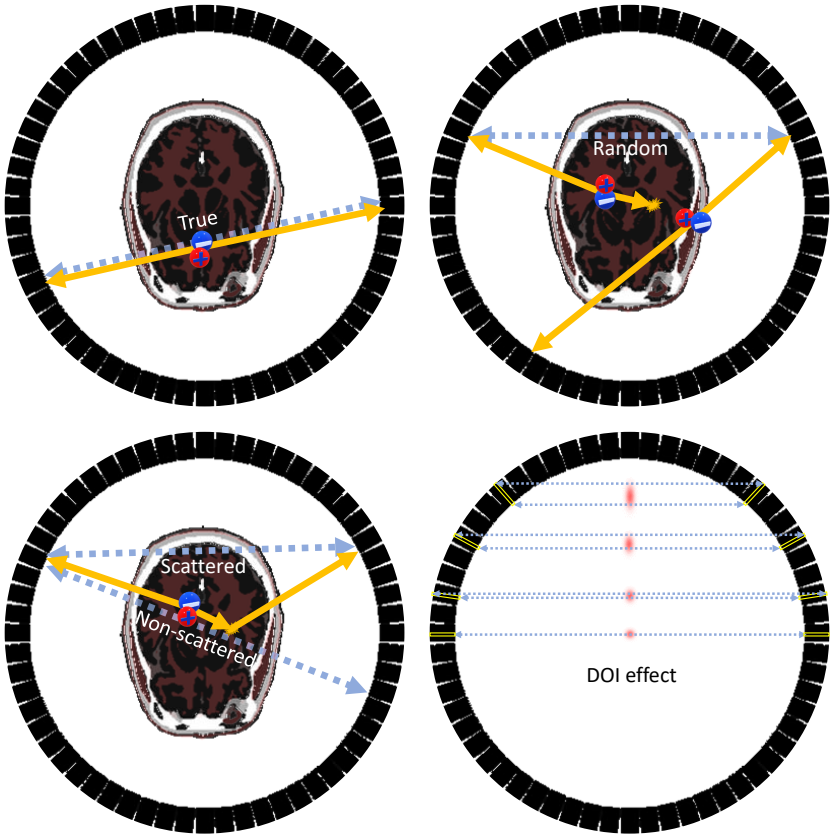

Figure 1. Graphical example of true (top-left), random (top-right) and scattered coincidences (bottom-left), and radial resolution loss of a point source caused by DOI effect (bottom-right).

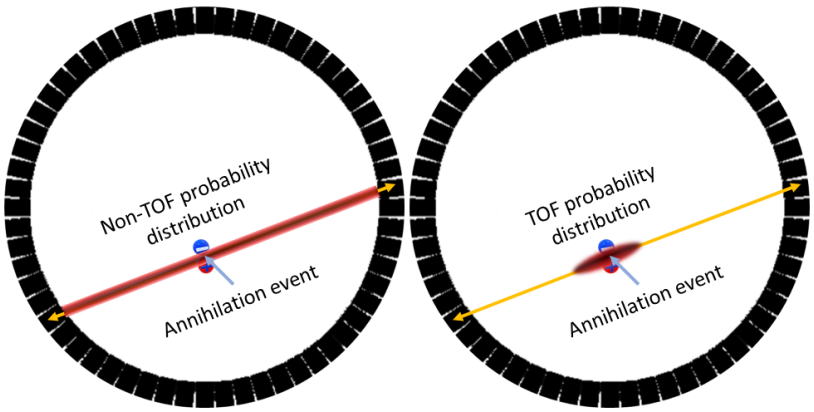

Figure 2. Scheme of the TOF information effect. Including TOF information (right)in the reconstruction process translates the uniform probability of an event occurring somewhere along the LOR to a Gaussian probability with full width at half maximum (FWHM) given by the CRT between both detectors.

- The photosensor, optically coupled to the scintillator crystal, generates an electronic pulse when a gamma photon is detected in the scintillator.

- The electronic circuit processes the electronic signal to obtain physical information about the detected gamma rays, and identify the coincidences needed for PET imaging.

2.1 Scintillation crystals

The scintillation detectors match PET needs with a reasonable trade-off between efficiency, energy resolution, and time resolution, hence they have been widely implemented. In a scintillation material, any gamma photon interaction results in an energy-proportional emission of photons in the visual energy range. Currently, there are different types of scintillation crystals (organic and inorganic in solid, liquid, and gaseous forms) [26]. In PET scanners, we commonly find solid inorganic crystals because of their high stopping power (defined as the energy lost per unit length) and high light response [27, 28]. In the context of PET/MR, scintillation materials do not present any contraindication.

The intrinsic efficiency of the scintillator is a function of its effective atomic number (averaged over its composition), its density, and the crystal thickness. The energy resolution is closely related to the photons emitted and their transport through the crystal. The number of photons emitted is quantitatively measured as the light yield, and the transport of photons is dominated by the refractive index of the material (the lowest, the better). The emission spectrum of the scintillator should match the photosensor sensitivity for optimal performance. It is also important to cover the crystal with reflectors to guarantee that a high fraction of the light can be collected. The time response in the scintillator has two main components: a fast-rising signal and a slow-falling signal (decay constant) that determines the time resolution [29]. In PET detectors, the scintillation crystals are usually pixellated to improve the spatial resolution of the photon interaction point. Some manufacturers have developed monolithic scintillators too [30–32].

Lutetium-based scintillators LSO (Lu_2SiO_5) [33] and LYSO ($Lu_{2(1-x)}Y_{2x}SiO_5$) have become the trend in modern PET scanners because of their high stopping power, high light yield, and fast time response [28]. Other proposed materials are GSO (Gd_2SiO_5) [34, 35], since it has a low price and acceptable performance, making it suitable for long axial field-of-view (FOV) scanners, and GAGG ($Gd_3(Ga, Al)_5O_{12}$) or $LaBr_3$ [28], because of their superior performance. NaI(Tl) was the first scintillation crystal used in PET [36], but it was soon substituted by other materials with higher stopping power, such as BGO ($Bi_4Ge_3O_{12}$). In contrast, BGO has a low light output yield compared with NaI(Tl) and other scintillators [19]. In recent times, BGO has drawn the attention of researchers since it offers the possibility of using Cherenkov radiation to improve the coincidence time resolution in TOF-PET scanners [37, 38]. In table 1 we summarize the main properties of these materials. Other authors also proposed cheaper detectors with lower sensitivity and high coincidence time resolution based on Cherenkov radiation, such as plastic scintillators [39] or PbF_2 [40].

2.2 Photosensors

The photosensor converts the optical response of the scintillator to an electrical signal that is later processed. To perform energy spectroscopy of the incident gamma rays, this device must

Table 1. Main properties of common PET scintillators. Adapted from Yu et al. [28] and Lewellen et al. [19]. The refractive index for GAGG was taken from [41].

	NaI (Tl)	BGO	GSO	LSO	LYSO	$LaBr_3$	GAGG
Chemical Formula	NaI	$Bi_4Ge_3O_{12}$	Gd_2SiO_5	Lu_2SiO_5	$Lu_{2(1-x)}Y_{2x}SiO_5$	$LaBr_3$	$Gd_3(Ga, Al)_5O_{12}$
Z_{eff}	51	74	59	66	60	47	48
Density (g/cm^3)	3.67	7.13	4.89	7.4	7.2	5.3	6.63
Light yield (ph/keV)	41	9	10	31	30	67	54
Wavelength (nm)	410	480	440	420	420	370	540
Decay constant (ns)	230	300	60	40	41	25	94
Refractive index	1.85	2.15	1.85	1.82	1.81	1.95	1.90

maintain the proportionality between the light generated and the electrical pulse. Spatially sensitive photosensors are also required to provide the gamma interaction point in the detector [19]. Another quality required for the photosensors in recent multimodal PET/MR scanners is being able to operate under magnetic fields. The two most common photosensors employed in PET are photomultiplier tubes (PMTs) and silicon photomultipliers (SiPMs).

PMTs are made of a vacuum tube that enclosures three main parts: the photocathode, a sequence of dynodes, and the anode [26]. When the photons hit the photocathode, the electron response generated is amplified in the dynodes sequence, obtaining a signal in the anode proportional to the energy deposited in the scintillator. The PMT has been the reference photosensor for PET scanners since the beginning of the technique, but its disadvantages are encouraging the use of other photosensors in the field. Some of them are its sensitivity to magnetic fields [42], requiring special shieldings to make them compatible with MR [43], its bulky size, and its expensive cost because of their complex manufacturing process.

SiPMs have overcome most of the disadvantages of PMTs: they have similar gain, fast response, low manufacture expenses, possible one-to-one coupling with the scintillation pixels, and especially, compatibility with MR scanners [44]. A few drawbacks of SiPMs are non-linear response or lower photon detection efficiency. Although SiPMs add noise due to thermal factors, which should be considered when working together with MR, with correct temperature controls, SiPMs are the best option to replace PMTs in combined PET/MR scanners. SiPMs are conformed of a matrix of avalanche photodiodes (APDs). The APDs are semiconductor detectors that create an avalanche of hole-electron pairs when a visible or ultraviolet photon is absorbed in a depleted region. The APD itself can be used as a photosensor, but they suffer from high noise in the amplification process, compromising the temporal resolution. For this reason, in SiPMs, the matrix of APDs works on Geiger mode, in which they detect single photons when a signal is generated over a threshold [45]. The multiple cells can provide a proportional signal to the input light by summing all the activated cells. Currently, SiPMs have displaced PMTs in most of the modern TOF-PET systems [46–51] and combined PET/MR scanners [52–56]. However, there is still space for other MR-compatible photosensors, such as APDs [57, 58], being an active research field.

2.3 Electronics

When a photon interacts with the detector and deposits an amount of energy above a given threshold, the electronics will detect the event (single event) and from the electronic pulse generated in the photodetector, the electronic circuit behind will obtain information about the time stamp, deposited energy, and location of the gamma photon interaction [26]. To avoid time-energy walk effects, the time stamp can be obtained analogically with the help of a constant fraction discriminator (CFD) that estimates the moment in which the pulse exceeds a constant fraction of its maximum amplitude. The total charge accumulated in the photosensor is used to estimate the energy of the photon. Usually, there are low- and high-energy discriminators to discard events far from the 511 keV peak. The gamma interaction point is estimated by weighting the multiple outputs of a position-sensitive photosensor.

First PET detectors used a quadrant-sharing scheme, where up to four PMTs would read the light produced in an array of scintillators, and the measurement of the light shared by each PMT allows to place the gamma interaction in the XY plane of the detector [59]. In order to reduce the number of electronic signals to be read, these were multiplexed by means of resistor networks. Most modern PET scanners today, however, used a separate SiPM photosensor for each small scintillator element, as it is the case in the Siemens Biograph Vision PET/CT scanner (Siemens Healthineers, Erlangen, Germany) [60], and read every signal from each separated photosensor. This increases the light received by each individual photosensor and allows for instance for improvements of the timing information and energy resolution of the newest scanners. This comes at the price of a many-fold increase in the number of signals that need to be read, decoded, and digitized. Dedicated ASIC electronics are at the heart of most modern PET scanners, in order to keep the cost of the electronics under control.

Recalling the interest of detecting pairs of annihilation photons, single events are processed, either by a hardware coincidence unit, or by a software coincidence algorithm, to identify pairs of events within a time window of the order of a few nanoseconds. This is what we call electronic collimation, and we call a coincidence event to every pair of single events within the time window. The TOF is very useful to improve the decay location within the LOR, and the CRT has been continuously improving over the last years, being now close to 200 ps in commercial clinical scanners [61].

3 PET/MR configurations

Since the first PET/MR prototype was developed in 1997, several approaches have been considered to acquire PET and MR images in a single scanner [62, 63], although their overall designs are substantially different. They are normally categorized into sequential or simultaneous systems, the last category including insert-based and integrated PET/MR systems.

3.1 Sequential PET/MR

The first MR-compatible PET systems used PMTs coupled to scintillating crystals to detect gamma rays and amplify the signal. However, PMTs are overly sensitive to the static fields used in MR, making the data compress on one side of the detector [64]. The solution was to locate the PMTs

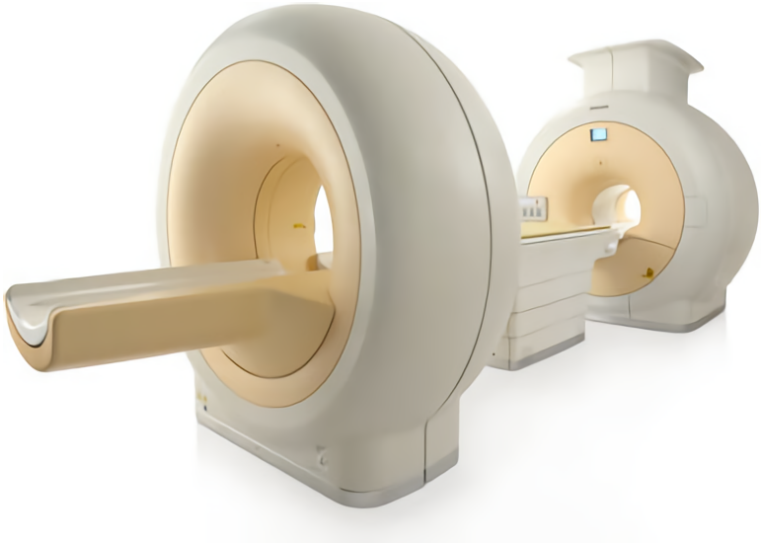

Figure 3. Commercially available Philips TF Ingenuity sequential PET/MR scanner: PET and MR scanners placed in the same room but maintaining enough distance to avoid electromagnetic interference. Image courtesy of Philips Healthcare.

outside the magnet and couple them to the scintillating crystals placed inside the scanner by using long optical fibers. This structure was used to simultaneously acquire for the first time PET images and 31P NMR spectra from isolated, perfused hearts and performing in vivo rat brain studies [65]. Multiple improvements were proposed afterward, but these evolutions demonstrated limited performance and were used only for pre-clinical imaging studies in small animals [66]. Actually, the first PMT-based human PET/MR scanner -the Philips TF Ingenuity (Philips Healthcare, Amsterdam, Netherlands)- allowed only sequential imaging. This scanner was composed of PET and MR scanners placed in the same room but maintaining enough distance to avoid electromagnetic interference (Figure 3). Data were acquired from each modality independently and posteriorly fused using software in a post-processing step. Nevertheless, this approach was not able to solve misalignment issues with moving organs. The first two clinical whole-body PET/MR systems were installed in 2010 [8].

3.2 PET/MR inserts

Early approaches for the advance of combined PET/MR scanners started by developing PET inserts that were compatible with already existing high-field animal MR systems [67–70]. PET inserts are basically a supplement to the MR scanners consisting of radially arranged LSO detector modules that could be coupled inside the bore of the MR scanner. The development of APDs allowed these PET detectors to be positioned in the bore of the MR scanner, and thus enabled simultaneous data acquisition.

At the same time these advancements in the preclinical PET/MR scanners were taking place, and with a focus on developing a completely integrated PET/MR scanner in the future, Siemens first designed several prototypes of the so called BrainPET/MR scanner [71, 72]. The BrainPET consisted of a PET insert which was placed into a standard, slightly modified 3T MAGNETOM

Trio MR scanner, and demonstrated its ability to simultaneously image a human brain in a one-bed position with both PET and MR. The PET ring insert had an internal diameter of 36 cm in which two dedicated MR head coils optimized for minimal PET attenuation were positioned. As these scanners were never commercially available, only four BrainPET prototypes were installed around the world between 2006 and 2010.

3.3 Integrated PET/MR systems

Currently Siemens, General Electric (GE Healthcare, Waukesha, Wisconsin, USA), and United Imaging (United Imaging Healthcare, Shanghai, China) are the only vendors to offer a fully integrated whole body and simultaneous acquisition PET/MR system. As the PET detector is integrated within the MR gantry –between the gradient and the radiofrequency coils–, these hybrid scanners allow for completely simultaneous PET and MR acquisitions. Contrary to what happens in simultaneous systems based on PET inserts, the PET detector is completely integrated and not noticeable from outside the gantry, and does not use any space in the bore, maintaining a 60-cm wide diameter bore (Figure 4). This full PET and MR integration allowed for the whole-body application of PET/MR systems.

In this sense, Siemens designed the first PET APD detectors that permitted the full integration of PET and MR while maintaining the performance of each modality, and introduced the first fully integrated whole-body MR-PET scanner, called Biograph mMR [57]. The Siemens Biograph mMR system received the CE mark and FDA approval in 2011 and was the first company to offer simultaneous PET/MR acquisitions, with the first systems based on APDs installed in 2010 [73–75]. The actual architecture design also included integrated cooling features to guarantee optimal PET performance, as well as dedicated shielding to remove magnetic field interfering PET data. Nonetheless, APDs temporal performance is slower than that of PMTs, therefore, limiting the use of these detectors in TOF applications.

General Electric decided to focus its PET/MR developments on SiPM, which proved to be successful in combined PET/MR applications [76]. Eventually, General Electric introduced the GE SIGNA TOF PET/MR, which received its 510K clearance and CE mark in 2014, becoming the first whole-body integrated PET/MR scanner with TOF capabilities in the market [77].

Later on, United Imaging joined the effort in developing combined PET/MR systems, integrating the strengths of next-generation SiPM-based detectors with TOF capabilities (480 ps timing resolution) and a 3T MR in the uPMR 790 HD TOF PET/MR system. This scanner received FDA clearance in 2019.

4 PET image correction and reconstruction in PET/MR systems

Annihilation photons in PET are subject to both attenuation and scatter as they travel through matter [78–81]. Consequently, the amount of detected photons in each LOR is reduced. Additionally, the photons can be scattered due to the Compton effect but still reach the PET detectors. Precise corrections for both physical phenomena are required to produce quantitative images reflecting the true spatial distribution of the radiotracer.

Figure 4. Integrated PET/MR Scanners. Commercially available integrated PET/MR scanners: Siemens Biograph mMR (top), GE SIGNA PET/MR (middle) and UI uPMR790 PET/MR (bottom). Images courtesy of Siemens Healthineers, General Electric Healthcare, and United Imaging Healthcare.

4.1 Attenuation correction

Loss of counts due to attenuation and scatter increases image noise, artifacts, and distortion. Figure 5 shows how, without AC, significant artifacts may occur on PET scans including:

- prominent activity at body surface edges due to relative lack of attenuation at the surfaces compared to deeper structures.
- distorted appearance of areas of intense activity (e.g., urinary bladder) due to variable degrees of attenuation in different directions of activity originating from these areas.
- diffuse and relatively increased activity in tissues of relatively low attenuation (e.g., lungs).

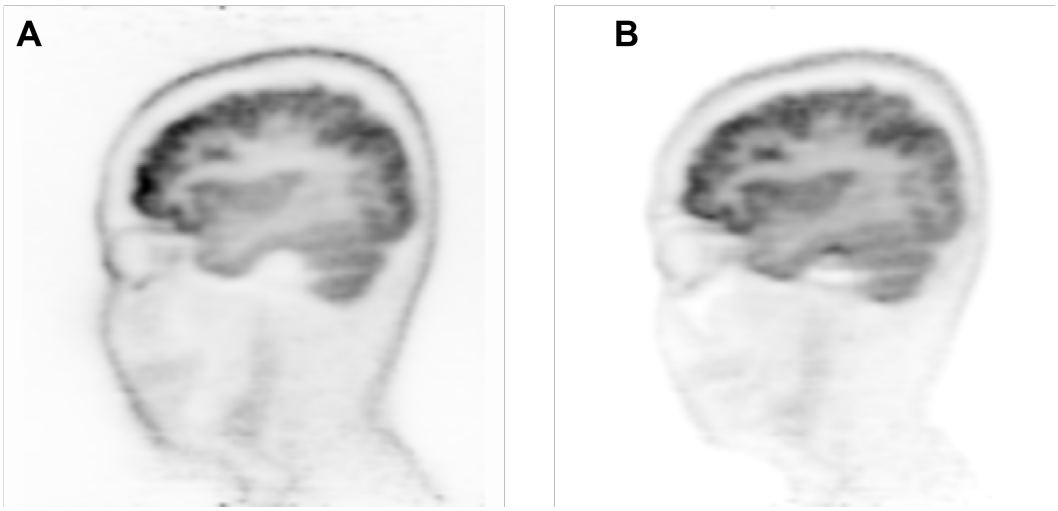

Figure 5. Sagittal slice of a 18F-FDG PET study showing the reconstructed image without attenuation correction (A) and with attenuation correction (B). Note the background noise, the prominent uptake at the skin and the levels in the frontal lobe.

The measurement along each LOR can be corrected if the properties of the object are known [82]. Nevertheless, constructing PET AC maps for use in simultaneous PET/MR systems is challenging because no direct relation exists between linear attenuation coefficients (μ) and MR signal intensity [83], contrary to what happens with AC maps and the intensity of CT images [84]. Additionally, treating bone as soft tissue in MR-derived AC maps for PET/MR AC leads to a substantial underestimation in the analysis of PET tracer distribution [85].

In the case of the fully integrated PET/MR scanners accessible in the market, AC maps are usually generated from the MR data acquired using a "Dixon Volumetric Interpolated Breath-hold Examination" (Dixon-VIBE) sequence or a "Liver Acquisition with Volume Acceleration-Flexible" (LAVA-Flex) sequence. Typically, four classes of tissue are segmented (background, fat, lung and soft tissue) based on the Dixon-VIBE or LAVA-Flex data, and discrete linear attenuation coefficients are allocated to each of these classes. Recent developments added bone information over these maps based on atlas. The main drawback of these methods rests in the inaccurate assignment of bone as soft tissue in the four-class segmentation approach, leading to a significant bias in the PET

measurements. Similarly, assigning discrete and unvarying linear attenuation coefficients does not describe the entire diversity of attenuations in actual tissues.

Hence, most of the early developments focused on trying to solve this issue in the head and neck [86, 87], principally differing in the type of semantic representation –segmentation [88, 89] or atlas-based [90, 91] methods– used to explain the resulting AC maps. In this setting, MR-based pseudo-CT synthesis (estimation of the patient-specific CT from the acquired MR data) can assist in the generation of continuous, more detailed and accurate MR-based AC maps, with a comparable quality to those AC maps obtained from the patient-specific CT, and several groups worked towards this direction.

Several different early developments started trying generating a head & neck pseudo-CT and following diverse approaches such as image registration and pattern recognition techniques to match MR and CT data [92], atlas-based methods grounded on non-rigid registration of a parametric atlas [90], enhanced approaches based on non-rigid registration of a non-parametric multi-atlas followed by a label fusion step depending on patch similarity measures [93], or the use of Convolutional Neural Networks (CNNs) to synthesize pseudo-CT images [94], even using incomplete (head & neck MR images and restricted local portions of CT) databases [95]. An extensive assessment of several of these methods demonstrated that many are accurate enough for clinical practice [96].

Figure 6 illustrates a comparison among AC maps of the head and neck obtained from a real CT (Figure 6A), by using a segmentation by classes approach (Figure 6B) and a pseudo-CT synthesized employing the method described by Torrado-Carvajal et al. [91] (Figure 6C), in addition to their matching attenuation corrected PET images for each of these approaches (Figures 6D-F) and fused with an anatomical T1w MR image (Figure 6G-I). This figure shows how the PET image corrected using the AC map derived from the segmented image demonstrates a decrease in signal in the most internal side of the skull, along with frontal and occipital areas, because of the inaccurate estimation of the skull, whereas the PET corrected using the AC map derived from the pseudo-CT is more similar to that obtained with the AC map derived from the actual CT of the patient.

In view of these results, it seemed the MR-based AC challenge was solved in combined PET/MR scanners. Nevertheless, translating these same approaches to whole-body applications was not straightforward. The greater variability amongst subjects (i.e., morphology, body mass index, pathology, sex) makes it problematic to create and establish an atlas that satisfactorily describes the entire population. Additionally, the usage of the aforementioned approaches in other regions different than the head and neck entails an amalgamation of rigid and non-rigid registration (atlas deformation). Subsequently, most of these approaches present inadequate performance when applied to whole body AC [81, 97, 98]. Thus, several research efforts have been made in recent years to tackle this challenge.

For instance, preliminary efforts tackling with the pelvic region reported semiautomatic approaches relying on multiple MR sequences (Dixon and zero-echo-time (ZTE) images) to estimate a pseudo-CT from the combination of the MR sequences [99]. Still, these approaches required a manual correction stage throughout the bone segmentation, consequently restricting its clinical applicability in real scenarios. As an alternative to classical atlas-based methods and the initial semiautomatic solutions, and considering the growing awareness in deep learning (DL) approaches, the use of CNNs for MR-based AC maps synthesis started to be studied for pelvic studies. Several proposals focused on estimating multiparametric MR models to synthesize pseudo-CT images of

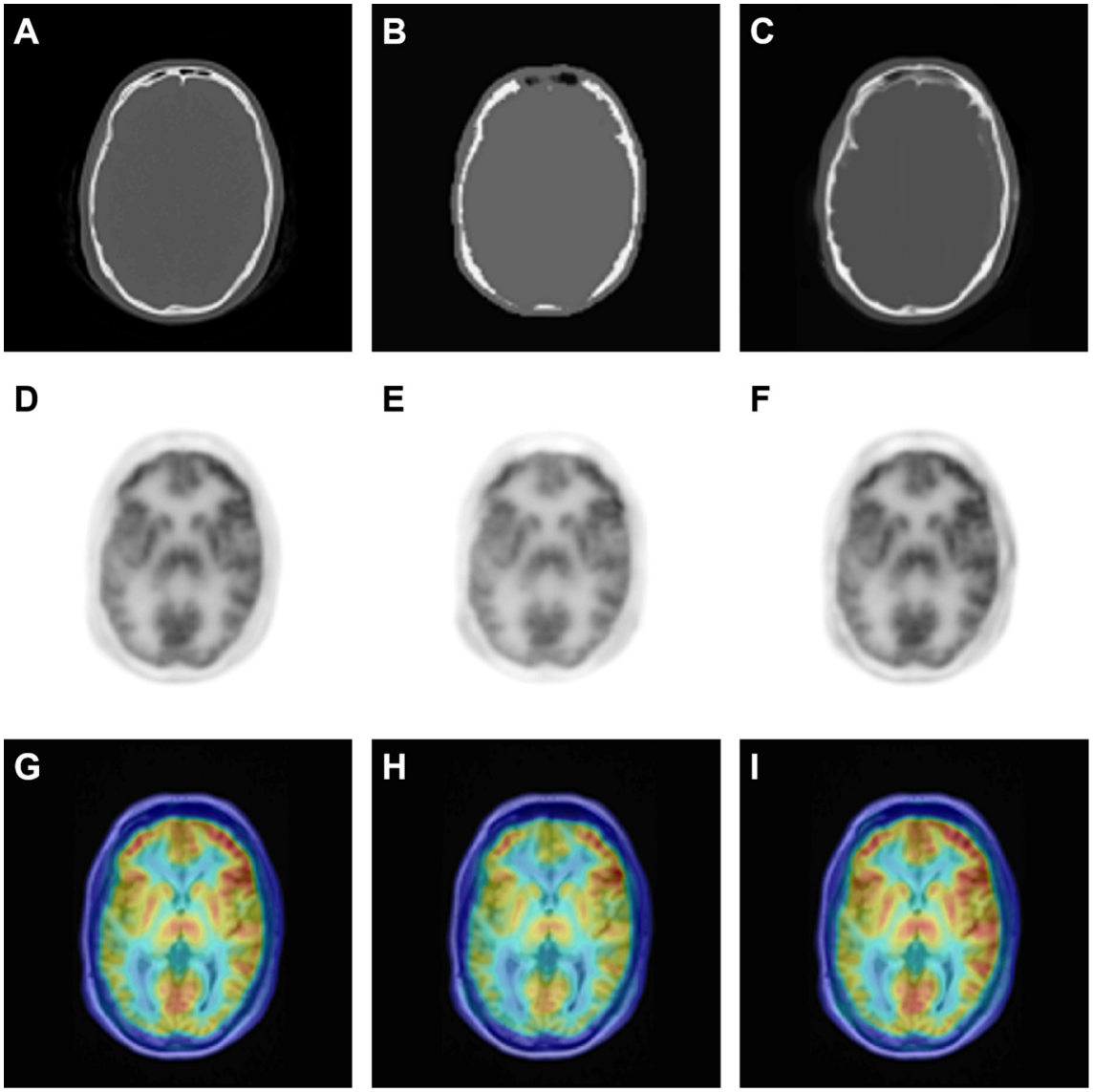

Figure 6. Axial slices of AC maps of the head and neck obtained from a real CT (A), and from MR images with a method based on segmentation by classes (B) and with a pseudo-CT synthesis method (C) , as well as the 18F-FDG PET study images corrected with each of these methods (D-F) and the representation of each of these PET images fused with an anatomical MR T1 image of the patient (G-I). From Torrado-Carvajal et al. [81].

the pelvis based on Dixon images and additional ultra-short-echo-time or ZTE images [100]. While their preliminary results were promising, these approaches present the drawback of requiring dedicated MR sequences that involve added MR acquisition times. Nevertheless, the rapid advancement in CNN architectures and flexibility derived in novel developments that could map between the four MR Dixon-VIBE images (water, fat, phase and counterphase) and CT images, generating precise pseudo-CT images of the pelvis without the need for acquiring extra sequences [101, 102]. The main challenge of these approaches was that neglecting air pockets in the pelvis AC maps could

lead to inaccuracies in reconstructed PET images. However, these innovative methods based on CNNs even showed the capability of predicting air pockets and include them in the AC maps [103].

Even the described AC methods presented some challenges when applied to chest imaging, due to its high anatomical complexity and inherent cardiac and respiratory motion [104]. On the one hand, most of the approaches neglected mapping the continuous distribution of attenuation coefficients inside the lungs, which fluctuates both within a given subject and among subjects, and depend on the breathing cycle, the lung inflation, gravitational dependence, and pathology. Although MR was shown to be of help when estimating continuous lung coefficients in MR-based AC [105]. On the other hand, respiratory and cardiac motion can lead to misalignments between the AC map and PET, resulting in improper PET data quantification, for instance, in the quantification of cardiac perfusion and metabolism [106, 107]. Deeper insight on these challenges will be covered in the motion correction section.

There are other factors that should be mentioned in the context of MR-based AC. In integrated systems, radiofrequency MR coils can also attenuate gamma ray photons when placed between the subject and PET detectors. Equipment manufacturers provide attenuation maps for most coils so that they can be automatically combined with the human maps in the AC procedure. Moreover, while both arms should be considered in the AC map, they are truncated in the FOV in the MR images, causing an underestimation of the tumour activity by 10 to 25% [108]. Nevertheless, the truncated arms can be inferred using the maximum-likelihood reconstruction of attenuation and activity procedure [109]. It should be also noted that all these methods and anatomical areas are subject to distortions in the MR-based AC maps due to the presence of metallic implants. To answer the issues derived from imaging patients with implants, MR images and AC maps can be improved by using specialized sequences that allow imaging near metallic implants (MAVRIC or SEMAC sequences), recovering the lost signal by means of image post-processing methods, or completing the AC map based on joint estimation of emission and attenuation [110, 111].

4.2 Scatter correction

In PET, scatter typically denotes Compton scattering. In this process, one or both annihilation photons interact with an electron, losing some energy and changing their direction [26]. If the scattered photon is eventually detected, the resulting LOR will not correspond with the original one (see figure 1), resulting in a smooth background and artifacts that reduces the contrast of the images and may affect especially when many of these events are accumulated [112–114]. In clinical acquisitions, the proportion of scattered events may be up to the 50% [24, 25, 115], making it a very significant correction. Many modern scanners work with a narrow energy window around 511 keV (usually from 400 to 650 keV [34, 57, 70, 72]) to discard most of the scatter events. Nevertheless, scatter corrections are still required even with a narrow energy window.

Multiple approaches have been proposed in the literature to perform scatter corrections in PET. Their main differences are the way in which the scatter is estimated. Once calculated, the scatter contribution may be subtracted from the data or added to the forward projection model. A few authors implemented experimental approaches based on multiple energy windows (spectral approaches) [116–118]. The basic hypothesis is that the whole energy spectrum of the scattered counts or at least the integral of that spectrum –from the lower energy discriminator to the upper one of the photopeak window– could be estimated given a big enough number of events below

and above the photopeak. These approaches typically include supplementary information to obtain potentially further accurate outcomes, aiming at withdrawing the scattered counts, voxel by voxel.

In the past, some authors proposed analytical methods based on fitting a Gaussian function to the scatter tails at the edge of each projection (assuming this contribution was mainly scatter) [116]. This approach obtains good results in brain imaging, as the activity and the scattering medium is homogeneously distributed and focused on the center of the FOV, resulting in a simple gradually varying scatter distribution. However, this approach fails in whole body applications, as the scatter tails obtainable for fitting are way shorter (since the body occupies a bigger part of the FOV) and the scatter distribution comprises further structures.

The most commonly used method has been the single scatter simulation (SSS) [119–121]. SSS includes a realistic model of scattering based on the activity emission map and the attenuation map (either obtained from CT or MR) to integrate the single scatter contribution of all the voxels in every LOR. Since scatter contribution is smooth, the uncertainties of MR-based attenuation maps are way less relevant than for the attenuation correction. The SSS needs a global scale factor that is usually obtained with tail fitting strategies based on the fact that no true activity is expected in the edges of the FOV and only scatter counts may be present [122, 123]. However, tail fitting may result in halo artifacts around high organ-to-background regions, such as the bladder or kidneys, or create biased estimations if there are arms or other sources in the border of the FOV [113, 114]. Other intrinsic drawbacks are the missing detector modeling [124], or multi-scatter events that may account from 15 to 40% of total scattered events [24, 25], resulting in wrong contrast values [125]. Some of these drawbacks were solved by Watson et al. in the most recent version of SSS [126], adding double scatter simulation (DSS) and considering all the physics in the scanner to estimate the scatter global scale.

Pure Monte Carlo (MC) simulations are considered the most accurate method for scatter estimation [116, 124, 127, 128], and might become a substitute to overcome the drawbacks of SSS thank to the higher computational power of current graphics processing units (GPUs) and clusters of central processing units (CPUs) [124, 129]. To improve SSS robustness, some authors combined MC global scaling factor from a quick simulation with the SSS scatter distribution [130, 131]. MC methods were combined with variance reduction techniques to increase the computational performance [116, 128], but it was not until GPU parallelization that they were considered for practical use [124, 127].

DL methods may help to speed up and enhance the scatter correction performance of the aforementioned methods. A few authors relied on DL methods to achieve quick MC-equivalent sinogram scatter estimations using the promts and attenuation sinograms or SSS estimation as input [132–135]. Long MC simulations are treated as the gold-standard output targeted by the network in order to speed up the prediction, and the network estimation is incorporated in standard reconstruction algorithms. Prats et al. proposed a different approach based on a gradient boosting decision tree to tag true and scatter events [136], despite they did not achieve MC scatter fraction values. Image post-processing approaches have been proposed as well, in which a non-corrected PET image is transformed into a corrected PET image, usually joining attenuation and scatter correction in the process [137–140]. These promising results provide a practical solution for standalone PET scanners in the clinic. Nonetheless, DL methods are susceptible to outliers, resulting in artifacts, quantification errors, missing lesions or false-positive results, so special

attention must be taken in these approaches [140].

4.3 Motion correction

Motion is difficult to avoid in long lasting PET studies, degrading the overall image quality and offsetting the advantage of employing a high-resolution scanner. Typical motion sources come from the inherent difficulty of the patient to stay still for long periods of time (voluntary or involuntary movement), but more specifically from physiological processes such as respiratory and cardiac motion. As the PET data take many minutes to acquire, the motion effects of the entire respiratory cycles or cardiac cycles are averaged together in the final reconstructed image. Figure 7 shows how, without motion correction, significant artifacts which may occur on whole-body PET. These effects result in a:

- blurring of the final PET images and severe artifacts when motion has large amplitude, resulting in spatial resolutions close to 1 cm.
- mismatch between the PET and MR data, which can even produce improper AC during PET reconstruction, especially at soft tissue, bone, and lung interfaces.

As a potential solution, in combined PET/MR scanners, the simultaneously acquired MR data can be employed to derive high-temporal-resolution motion estimates, removing the need for other external tracking systems.

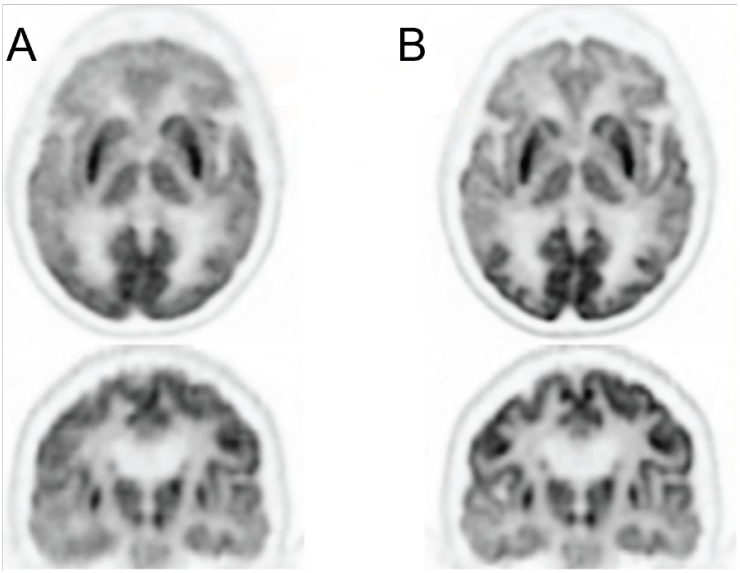

Figure 7. Axial (top) and coronal (bottom) slices of a 18F-FDG PET study showing the reconstructed image without motion correction (A) and with rigid motion correction (B). Adapted from Spangler-Bickell et al. [141].

Numerous methods have been developed in the case of neurological PET studies [142, 143], starting with simple methods to realign individual frames (shorter time reconstructions) to a fixed reference position and summing all of them to generate the final single volume. However, these methods neglect the availability of simultaneously acquired MR data that could be used to track motion. In this sense, several approaches have been assessed in brain imaging, such as using the

information extracted from echo planar imaging (EPI) series or embedded cloverleaf navigators (CLNs) [144], or the use of MR navigators sampled between other protocolled MR sequences during simultaneous PET/MR brain scanning [145].

Recent studies have demonstrated how a failure to perform motion correction results in large artifacts among high-motion subjects and how correcting for motion alleviates most of the bias, and specifically correcting for inter-frame motion delivers most of the benefit [146].

Whole-body PET imaging, and in particular cardiac imaging, is restricted by the degradation due to motion. Due to respiration, the diaphragm and the liver move in the range of 7–28 mm and 5–17 mm, respectively, and, during free breathing, the heart moves in the range of 4.9–9 mm due to its own heartbeat and to the movement of the chest due to respiration. These motions can be managed by using gating, which can remove most of the artifacts but at the cost of increased noise in the final reconstructed images and, sometimes, increased acquisition times to counteract this SNR loss.

Early accurate motion estimation techniques were developed using tagged MR and applied to PET motion correction [147]. Tagged MR enforces a spatially periodic magnetization pattern (tags) prior image acquisition; after the tagging pulses, the magnetization pattern is maintained over a specific time and changed by motion, which can be measured in the MR images.

Several recent MR-based motion correction methods for cardiac PET data included specifically designed MR protocols to account for motion during the examination [148–150]. Nevertheless, these images present a lack of soft tissue contrast and/or spatial resolution that avoids using these images for other tasks rather than motion estimation (i.e., for diagnostic purposes). Thus, the inclusion of these additional images usually results in prolonged examination times, as MR images acquired during the PET/MR study are just acquired for the sake of motion correction, and diagnostic MR images have to be acquired once the PET acquisition is over.

Most current approaches have tried to avoid prolonging the MR acquisition protocol. On the one hand, several methods have attempted to either extract motion estimates from respiratory navigated 3D MR acquired images based on radial phase encoding [151], or from image-navigators (iNAVs) to track cardiac movement being feasible in single phase whole heart imaging [152]. This type of MR acquisition protocols demonstrated allowing for both high resolution 3D structural data and extremely precise nonrigid motion estimation without an increase in overall scan times, leading to a strong enhancement in both MR and PET image quality and guaranteeing a precise assessment of radiotracer uptake. On the other hand, newer methods have tried to benefit from the use of CNNs to estimate cardiac motion; for instance, CarMEN, an unsupervised 3D cardiac motion estimation network for deformable motion estimation from 2D cine MR images [153]. This is an example on how CNNs allowed for a novel framework where motion can be estimated from cine MR volumes, despite each time frame being strictly a 2D stack of independently acquired sections, rather than an actual 3D simultaneously acquired volume.

4.4 Image reconstruction

The goal of image reconstruction in PET is to obtain the most accurate representation of the radiotracer distribution inside the patient. Different methods have been proposed over the years in order to translate the emission-detected events into the 3D image space. Most authors have separated reconstruction methods into analytical and iterative (or statistic) methods [154–156], although it

is worth mentioning the recent incorporation of DL techniques either for direct reconstruction or mixed reconstruction with existing methods [157–160].

4.4.1 Analytical methods

A fundamental tool of these methods is the Radon transform [161], which defines the projection space (also called sinogram in PET), where the PET data are found. To recover the image from the projection space, the central-section theorem (or Fourier slice theorem) plays a major role. This theorem correlates the Fourier transform (FT) of each 1D projection with the radial profile through the 2D FT of the image at the same angle [162]. The most widely used analytical method is the filtered-backprojection (FBP) algorithm [155, 161, 162]. Other analytical methods, such as the backprojection-filtering (BPF) [163], or 3D adaptations of the FBP [164] have been also developed. Recently, Lopez-Montes et al. have introduced a reconstruction method based on a more accurate model of the system response matrix (SRM) using a pseudoinverse transformation that provides higher resolution than the traditional FBP [165, 166].

In general, analytical methods assume idealized linear image projection models of the system with additive gaussian noise and complete data that can be mathematically inverted or pseudo-inverted to recover the activity distribution. These assumptions are not good approximations for PET scanners, resulting in artifacts and quality loss in the reconstructed images. For instance, the physical effects that degrade the image quality are not modeled in the FBP, thus limiting the resolution that can be recovered from this method. In [167], the sinograms were deconvoluted to restore the lost resolution because of intrinsic PET effects. The problem as it has been stated so far is ill-posed, and small changes in the data (for example, because of Poisson noise, random coincidences, scatter events, etc.) may lead to big changes in the image. Low-pass filters have been commonly used to remove high-frequency noise. A few common examples are the ramp filter, the Hamming filter or the Shepp-Logan filter [162]. PET scanners are also conformed of discrete detector units with gaps in the projection domain from two contiguous blocks, which result in discrete data with small gaps. This problem is partially solved using "inpainting" techniques to fill in the empty spaces, or other sophisticated strategies [168]. Most of the analytical methods are derived from 2D formulation, whereas PET data are gathered in 3D. Although some authors adapted the problem to 3D [164], it is very common to use 2D rebinning techniques followed by 2D reconstruction [165, 166, 169–172]. Analytical methods produce noisier images than iterative methods. In contrast, it is important to remark that analytical methods are usually faster, being a linear mapping between the data and the reconstructed images, and they are typically preferred for performance assessment of PET scanners [173, 174].

4.4.2 Iterative methods

Iterative methods focus on the optimization of an objective function, searching for the image that better matches the data through small steps. These algorithms include a SRM that relates the data domain with the image domain, the objective function to be optimized, a statistical model of the noise in the data, and an iterative algorithm that estimates the image evolution toward the convergence of the optimal solution [163, 175].

The SRM is of great importance to obtain the best image quality for our system, and it must accurately model the most relevant physical processes involved in the emission, transport,

and detection of radiation in our acquisition system [156]. The most important considerations are the positron range, the non-collinearity of annihilation photons, photon interactions with the patient body (attenuation and scatter), random coincidences, the scanner geometry, and the detector response (such as the depth of interaction in the detectors (DOI), inter-crystal scatter, or intrinsic efficiency). Usually, the matrix is factorized and attenuation correction, scatter events, random coincidences, and the normalization (sensitivity of a given LOR) are corrected separately [176, 177].

SRMs have been estimated using either analytical, experimental, MC, or hybrid approaches. Analytical approaches are based on geometrical projection models [54, 178–181], analytical models of the physical processes [182–185], or convolutional kernels usually referred to as Point Spread Function (PSF) [186]. The PSF is a widely used method for SRM modeling [187], consisting of either image or projection blurring kernels applied as a convolution operation. These methods are fast, and they allow for on-the-fly calculations that drastically reduce the storage requirements of a precomputed SRM [156, 188, 189]. For this reason, they have been usually combined with experimental or MC estimations of the SRM to optimize the computational performance. In experimental approaches, point sources are acquired at different positions of the scanner FOV and the measured response is fitted to hand-crafted convolutional kernels either in the image [190–192] or sinogram domain [193–197]. In [198], the authors used narrower PSF for single crystal events identified by the detectors to increase image resolution. Other authors have benefited from MC methods to reproduce the SRM with long simulations. In this case, the SRM may be determined as an explicit matrix of probabilities relating to each voxel-LOR pair [199–203]. Since these matrices require high loads of memory storage, symmetries and SRM sparsity have been exploited to reduce the SRM size. Some authors applied PSF descriptions [185, 204–207], or wide tubes-of-response (TORs) [208–211] instead of simple projection models. Other approaches include separate positron range correction, which is included in the reconstruction as an image blurring kernel [212, 213].

The objective function and the optimization method used also play an important role in the final solution achieved. The first proposed algorithms, known as Algebraic Reconstruction Techniques (ART) [214], minimize the least-squares problem of the system. Later, a variation of the ART algorithm was proposed by Andersen [215], the Simultaneous Algebraic Reconstruction Technique (SART). One of the most successful algorithms has been the Maximum Likelihood Expectation Maximization (MLEM) [216]. Motivated by the stochastic nature of the emissions in PET and Single-Photon Emission Computed Tomography (SPECT), the objective function, in this case, is the log-likelihood of the Poisson model for the data and the projections, and the optimizer chosen is the expectation maximization [217]. The Image Space Reconstruction Algorithm (ISRA) [218] was presented to preserve non-negativity images and reduce the memory requirement of the MLEM. The MLEM was optimized with the Ordered Subsets EM (OSEM) algorithm [219], which reduces the reconstruction time by the use of a small set of data in every update. OSEM is the current standard in PET imaging. The use of subsets can be generalized to other optimizers to guarantee convergence, like [220] did for the ascent gradient algorithm in the Row-Action Maximum Likelihood Algorithm (RAMLA). The MLEM is presented as a particular case of RAMLA. In [221], both ISRA and MLEM were presented from the point of view of a gradient descent algorithm of a weighted least-squares objective function, with properly chosen descent steps. In terms of noise models, the weighted least squares can be viewed as the log-likelihood of a gaussian model of the noise. Inspired by the use of gradient-descent Stochastic Variant Reduction (SVR) algorithms in machine

learning [222], many authors have recently studied the application of these methods in PET imaging to avoid limit cycles when ordered subsets are implemented [223–227].

In general, iterative methods converge to noisy images if the number of iterations is not controlled. To avoid this, penalty functions (also called priors) are added to the objective function. The goal is to select the image that satisfies our expectations, preserving edges while imposing local smoothness. These methods are usually known as Bayesian or Maximum "a posteriori" (MAP) methods [228, 229]. One of these implementations is the Block Sequential Regularized Expectation Maximization (BSREM) [230, 231], presented as a globally convergent algorithm incorporating priors in RAMLA with the appropriate step size. Examples of the penalty functions are the quadratic function or the Huber functions [232], the Geman function [233], the relative differences prior (RDP) [233–235], the median root prior (MRP) [236, 237], total variation [238, 239], or patch-based priors [240]. In general, these methods are susceptible to proper hyperparameter selection, and their use in the clinic is still limited. Q.clear [241–243] is one of the currently available commercial software, based on BSREM and the RDP prior. In the Kernelized Expectation Maximization (KEM) method [244], the image is modeled with a linear combination of specific kernels based on features that can be obtained from statical images in dynamic frames [244–246] or anatomical images [247, 248]. KEM allows a more complex representation of the priors since spatially-variant dependence can be included, instead of fixed functions for the whole image. This method has also been proposed as a successful choice to incorporate DL within the image reconstruction process (see next section).

All of these components make iterative algorithms outperform analytical algorithms in terms of SNR [154]. The statistical model makes them more robust to noise and incomplete data, and together with the iterative scheme allows for non-linear considerations in the reconstruction workflow. They can also introduce geometrical properties and model physical processes in the SRM, thus making them more accurate and easily adaptable for 3D imaging [155]. Iterative methods are computationally intensive compared with the FBP, since each iteration requires a forward projection and a backward projection operation, whereas in FBP this step is performed only once. Nevertheless, nowadays computer power and GPU parallel computing allow for routine image reconstruction with iterative methods in short computation time [203, 249–251].

4.4.3 Deep learning methods

In image reconstruction of PET data, the application of DL has followed different strategies [157, 158]. So far, we can summarize them in direct reconstruction, physics-informed DL, and post-processing methods [160, 252].

Direct reconstruction consists in mapping from noisy data to the output image, thus learning the full transformation from the projection space to the image space [253–257]. This approach currently implies memory issues since both spaces are high dimensional, requiring reducing the problem to individual 2D slices and large data sets to train the model.

In physics-informed DL methods, a hybrid approach combining DL with known physics about the system (such as the projection/backprojection model, the PSF, etc.) is implemented. Different authors implemented a fixed backprojection step combined with learned filters [258] and an image postprocessing network [259]. In [260–262], a hybrid approach was implemented for TOF data using histograms based on the most-likely annihilation position, and [263] implemented a cycle-consistent learning-based hybrid iterative reconstruction method based on two networks mapping

from the backprojection to the reconstructed image and vice versa. These approaches may be classified as direct DL reconstruction methods by some authors since they minimally make use of the Radon transformation or simple backprojection instead of the traditional iterative methods. Other authors have embedded DL methods within image regularization in the image reconstruction process. One of the methods proposed is the implementation of a learned gradient prior in the MAP algorithm [264–268]. The Deep Image Prior (DIM) method introduced by Ulyanov et al. [269], which consisted in the use of a CNN without specific training for image denoising, was incorporated in the ML optimization by Gong et al. using MR anatomical information [270]. DIM has the advantage of using unsupervised learning based on the patient information to train the network during reconstruction, thus not requiring large training datasets. Other authors have also studied the implementation of DIM within the reconstruction [271, 272]. A CNN has also been incorporated within the KEM method [273], and eventually, it has been combined with DIM [274].

The third approach is performing image post-processing with DL methods after reconstruction to improve quality or denoising. One of the most attractive applications of DL is image denoising from low-dose PET to standard-dose PET [275–280], as it may reduce the radiation exposure of patients in PET studies. The advantage of this approach is that image pairs can be easily obtained by removing events from list-mode data of standard-dose acquisitions. Denoising is also challenging for gated PET images [281], where gates suffer from higher noise than static images and different noise levels among gates. Image quality improvement has also been achieved including MR inputs in the CNN training [282–285]. These approaches demonstrated that MR images helped to significantly decrease noise while improving resolution and preserving detailed structures. Other authors applied a CNN to correct positron range blurring in ^{68}Ga images [286, 287], or transforming non-TOF to TOF images [288]. In the previous section 4.2, we already mentioned similar post-processing DL approaches to correct attenuation and scatter in the image domain.

4.4.4 MR-guided and joint reconstruction

Several recent approaches have focused on using both classical image processing techniques as well as novel techniques such as CNNs to improve PET or MR imaging. Therefore, numerous methods appraised using the potential of simultaneous PET/MR imaging in procedures to improve the quality and information content of original data while reducing artifacts, accelerate imaging acquisition and reconstruction, or decrease the associated risk to the procedures.

Many proposals directed efforts on improving the quality and information content of original data while reducing artifacts, especially as PET imaging suffers from severe inherent resolution limitations which reduce its quantitative spatial accuracy and degrades PET images by partial volume effects. In this context, one of the most studied approaches, both for PET and MR, is super-resolution. Super-resolution imaging refers to a category of techniques that enhance the quality of the acquired images by boosting their apparent resolution. In this scenario, CNN-based super-resolution methods can generate high-quality images from those reduced-resolution ones. In this sense, we can find methods for intramodality image super-resolution in PET imaging [289], in MR imaging [290], but increasingly more taking advantage of the complementary information present in combined PET/MR images [291]. The latter methods proved how CNNs trained using combined data outperformed traditional methods by large margins. Related to super-resolution methods, we find denoising methods, which were already discussed in section 4.4.3.

Other methodologies have also centered on reducing MR acquisition and reconstruction times. This is mainly because, in a combined PET/MR scan, the MR image acquisition can be very time-consuming and take more time than the actual PET scan. Minimizing the time required for raw data acquisition or under-sampling the k-space can accelerate the acquisition, but this impacts the resulting quality of the MR images. In this sense, there still exist novel developments to improve the quality of the resulting MR images based on probabilistic models and other information theory-based methods [292, 293], while CNNs are also gaining leadership in dealing with these applications [294]. These methods were able to enhance image resolution without any hardware adjustments while decreasing overall scanning time.

Furthermore, in previous sections we have already discussed several other approaches focused on applying DL methods to correct attenuation and scatter (section 4.1 and 4.2), and reduce radiotracer requirements without sacrificing diagnostic quality (section 4.4.3) in integrated PET/MR systems.

5 Conclusions

Hybrid medical imaging modalities combine two modalities in a single scanner, providing rich anatomical and functional information in a single study, thus reducing burden to the patient, time and cost. Among these devices, PET/MR is the most promising one for clinical routine, but the combination of these two modalities has required complex technical developments, both in the hardware and in the associated data and image processing techniques. In this work we have reviewed the history of PET/MR development, describing the different technical issues that were confronted and how they were solved, with a special emphasis on instrumentation, and image reconstruction and correction.

Acknowledgments

We would like to thank the 6th Summer School on Intelligent Signal Processing for Frontier Research and Industry (INFIERI) and, especially, Aurore Savoy-Navarro and José del Peso, for inviting us to participate in such an amazing Summer School, where they offered us the opportunity to organize a hands-on session on ”Clinical Positron Emission Tomography/Magnetic Resonance Imaging: Acquisition and Quantification”. We acknowledge support by the Young Reserchers R&DProject Ref M2166 (MIMC3-PET/MR) financed by Community of Madrid and Universidad Rey Juan Carlos.

References

[1] Suetens P., *Fundamentals of medical imaging*, Cambridge University Press (2017).

[2] Beyer T., Townsend D. W., Brun T., Kinahan P. E., Charron M., Roddy R., Jerin J., Young J., Byars L., and Nutt R., *A Combined PET/CT Scanner for Clinical Oncology*, *J Nucl Med* **41(8)** (2000) 1369-1379.

[3] Townsend D. W., Carney J. P., Yap J. T., Hall N. C., *PET/CT today and tomorrow*, *J Nucl Med* **45(suppl 1)** (2004) 4S-14S.

[4] Vandenberghe S. and Marsden P. K., *PET-MRI: a review of challenges and solutions in the development of integrated multimodality imaging*, *Phys. Med. Biol.* **60** (2015) R115–54.

[5] Cal-Gonzalez J., Rausch I., Shiyam Sundar L. K., Lassen M. L., Muzik O., Moser E., Papp L. and Beyer T., *Hybrid Imaging: Instrumentation and Data Processing*, *Front. Phys.* **6:47** (2018).

[6] Raylman RR., *Reduction of positron range effects by the application of a magnetic field: For use with positron emission tomography*, PhD dissertation. The University of Michigan (1991).

[7] Shao Y., Cherry S. R., Farahani K., Meadors K., Siegel S., Silverman R. W., and Marsden P. K., *Simultaneous PET and MR imaging*, *Phys Med Biol* **42(10)** (1997) 1965.

[8] Muzic R. F. and DiFilippo F. P., *Positron Emission Tomography-Magnetic Resonance Imaging: Technical Review*, *Seminars in Roentgenology* **49(3)** (2014) 242-254.

[9] Sander C. Y., Hooker J. M., Catana C., Normandin M. D., Alpert N. M., Knudsen G. M., Vanduffel W., Rosen B. R., and Mandeville J. B., *Neurovascular coupling to D2/D3 dopamine receptor occupancy using simultaneous PET/functional MRI*, *Proceedings of the National Academy of Sciences* **110(27)** (2013) 11169-11174.

[10] Akeju O., Loggia M. L., Catana C., Pavone K. J., Vazquez R., Rhee J., Ramirez V. C., Chonde D. B., Izquierdo-Garcia D., Arabasz G., Hsu S., Habeeb K., Hooker J. M., Napadow V., Brown E. N., and Purdon P. L., *Disruption of thalamic functional connectivity is a neural correlate of dexmedetomidine induced unconsciousness*, *Elife* **3** (2015) e04499.

[11] Loggia M. L., Chonde D. B., Akeju O., Arabasz G., Catana C., Edwards R. R., Hill E., Hsu S., Izquierdo-Garcia D., Ji R-R., Riley M., Wasan A., Zürcher N., Albrecht D., Vangel M., Rosen B., Napadow V., and Hooker J., *Evidence for brain glial activation in chronic pain patients*, *Brain* **138(3)** (2015) 604-615.

[12] Zürcher N. R., Loggia M. L., Lawson R., Chonde D. B., Izquierdo-Garcia D., Yasek J. E., Akeju O., Catana C., Rosen B. R., Cudkowicz M. E., Hooker J. M., and Atassi N., *Increased in vivo glial activation in patients with amyotrophic lateral sclerosis: Assessed with [11 C]-PBR28*, *NeuroImage: Clinical* **7** (2015) 409-414.

[13] Ciesienski K. L., Yang Y., Ay I., Chonde D. B., Loving G. S., Rietz T. A., Catana C., and Caravan P., *Fibrin-targeted PET probes for the detection of thrombi*, *Molecular Pharmaceuticals* **10(3)** (2013) 1100-1110.

[14] Katsumi, Y., Racine, A. M., Torrado-Carvajal, A., Loggia, M. L., Hooker, J. M., Greve, D. N., ..., RISE Study Group., *Fibrin-targeted PET probes for the detection of thrombi*, *NeuroImage: Clinical* **27** (2020) 102346.

[15] Amorim, B. J., Torrado-Carvajal, A., Esfahani, S. A., Marcos, S. S., Vangel, M., Stein, D., ..., Catalano, O. A., *PET/MR Radiomics in Rectal Cancer: a Pilot Study on the Correlation Between PET-and MRI-Derived Image Features with a Clinical Interpretation*, *Molecular imaging and biology* **22(5)** (2020) 1438-1445.

[16] Torrado-Carvajal, A., Toschi, N., Albrecht, D. S., Chang, K., Akeju, O., Kim, M., ..., Loggia, M. L., *Thalamic neuroinflammation as a reproducible and discriminating signature for chronic low back pain*, *Pain* **162(4)** (2021) 1241-1249.

[17] Alshelh, Z., Saha, A., Morrissey, E., Kim, M., Knight, P., Albrecht, D., ..., Loggia, M., *Neuroinflammatory and functional connectivity signatures in radicular and axial chronic low back pain*, *The Journal of Pain* **22(5)** (2021) 604.

[18] Sander, C. Y., Bovo, S., Torrado-Carvajal, A., Albrecht, D., Deng, H., Napadow, V., ..., Loggia, M. L., *[11C] PBR28 radiotracer kinetics are not driven by alterations in cerebral blood flow*, *Journal of Cerebral Blood Flow & Metabolism* (2021) 0271678X211023387.

[19] Lewellen T. K., *Recent developments in PET detector technology*, *Phys. Med. Biol.* **53** (2008) R287–317.

[20] Daube-Witherspoon M., Pantel A., Pryma D. and Karp J., *Total-body PET: a new paradigm for molecular imaging*, *Br. J. Radiol.* **95** (2022) 20220357.

[21] Surti S. and Karp J. S., *Advances in time-of-flight PET*, *Phys. Medica* **32** (2016) 12-22.

[22] Vandenberghe S., Mikhaylova E., D'Hoe E., Mollet P. and Karp J. S., *Recent developments in time-of-flight PET*, *EJNMMI Phys.* **3** (2016) 3.

[23] Lecoq P., Morel C., Prior J. O., Visvikis D., Gundacker S., Auffray E., Križan P., Turtos R. M, Thers D., Charbon E., Varela J., de La Taille C., Rivetti A., Breton D., Pratte J-F., Nuyts J., Surti S., Vandenberghe S., Marsden P., Parodi K., Benlloch J. M. and Benoit M., *Roadmap toward the 10 ps time-of-flight PET challenge*, *Phys. Med. Biol.* **65** (2020) 21RM01.

[24] Adam L-E., Karp J. S. and Brix G., *Investigation of scattered radiation in 3D whole-body positron emission tomography using Monte Carlo simulations*, *Phys. Med. Biol.* **44** (1999) 2879–95.

[25] Ye T., Chai P., Gao J., Yun M-K., Liu S-Q., Shan B-C. and Wei L., *Investigation of scatter from out of the field of view and multiple scatter in PET using Monte Carlo simulations*, *Chinese Phys. C* **35** (2011) 1166–71.

[26] Knoll G. F., *Radiation Detection and Measurements*, *John Willey & Son* **Fourth edi.** (2011).

[27] Gonzalez-Montoro A., Ullah M. N. and Levin C. S., *Advances in Detector Instrumentation for PET*, *J. Nucl. Med.* **63** (2022) 1138–44.

[28] Yu X. Zhang X., Zhang H., Peng H., Ren Q., Xu J., Peng Q. and Xie S., *Requirements of Scintillation Crystals with the Development of PET Scanners* , *Crystals* **12** (2022) 12.

[29] Ljungberg M., Strand S-E. and King M. A., *Monte Carlo Calculations in Nuclear Medicine*, *Boca Raton: CRC Press* **Fourth edi.** (2012).

[30] Freire M., Gonzalez-Montoro A., Canizares G., Rezaei A., Nuyts J., Berr S. S., Williams M. B., Benlloch J. M. and Gonzalez A. J., *Experimental validation of a rodent PET scanner prototype based on a single LYSO crystal tube*, *IEEE Trans. Radiat. Plasma Med. Sci.* **7311** (2021) 1-1.

[31] Stockhoff M., Decuyper M., Van Holen R. and Vandenberghe S., *High-resolution monolithic LYSO detector with 6-layer depth-of-interaction for clinical PET*, *Phys. Med. Biol.* **66** (2021) 155014.

[32] Doss K. K. M., Mion P. E., Kao Y-C. J., Kuo T-T. and Chen J-C, *Performance Evaluation of a PET of 7T Bruker Micro-PET/MR Based on NEMA NU 4-2008 Standards*, *Electronics* **11** (2022) 2194.

[33] Melcher C. L., *Lutetium orthosilicate single crystal scintillator detector*, *United States Patent* **5,025,151** (1991).

[34] Wang Y., Seidel J., Tsui B. M. W., Vaquero J. J. and Pomper M. G., *Performance evaluation of the GE healthcare eXplore VISTA dual-ring small-animal PET scanner*, *J. Nucl. Med.* **47** (2006) 1891–900.

[35] Surti S. and Karp J. S., *Imaging characteristics of a 3-dimensional GSO whole-body PET camera*, *J. Nucl. Med.* **45** (2004) 1040-9.

[36] Robertson J. S., Marr R. B., Rosenblum M., Radeka V. and Yamamoto Y. L., *32-crystal Positron Transverse Section Detector*, *Report: Medical Research Center Brookhaven National Laboratory* (1972).

[37] Kwon S. I., Gola A., Ferri A., Piemonte C. and Cherry S. R., *Bismuth germanate coupled to near ultraviolet silicon photomultipliers for time-of-flight PET*, *Phys. Med. Biol.* **61** (2016) L38–47.

[38] Gundacker S., Martinez Turtos R., Kratochwil N., Pots R. H., Paganoni M., Lecoq P. and Auffray E., *Experimental time resolution limits of modern SiPMs and TOF-PET detectors exploring different scintillators and Cherenkov emission*, *Phys. Med. Biol.* **65** (2020) 025001.

[39] Moskal P., Kowalski P., Shopa R. Y., Raczyński L., Baran J., Chug N., Curceanu C., Czerwiński E., Dadgar M., Dulski K., Gajos A., Hiesmayr B. C., Kacprzak K., Kapłon Ł., Kisielewska D., Klimaszewski K., Kopka P., Korcyl G., Krawczyk N., Krzemień W., Kubicz E., Niedźwiecki S., Parzych S., Raj J., Sharma S., Shivani S., Stępień E., Tayefi F. and Wiślicki W., *Simulating NEMA characteristics of the modular total-body J-PET scanner—an economic total-body PET from plastic scintillators*, *Phys. Med. Biol.* **66** (2021) 175015.

[40] Razdevsek G., Pestotnik R., Krizan P., Korpar S., Consuegra D., Seljak A., Studen A. and Dolenec R., *Exploring the potential of a Cherenkov TOF PET scanner: a simulation study*, *IEEE Trans. Radiat. Plasma Med. Sci* (2022) 1-1.

[41] Kozlova N. S., Buzanov O. A., Kasimova V. M., Kozlova A. P. and Zabelina E. V., *Optical characteristics of single crystal $Gd_3Al_2Ga_3O_{12}$: Ce*, *Mod. Electron. Mater.* **4** (2018) 7–12.

[42] Vaquero J. J., Sánchez J. J., Udías J. M., Cal-González J. and Desco M., *MRI compatibility of position-sensitive photomultiplier depth-of-interaction PET detectors modules for in-line multimodality preclinical studies*, *Nucl. Instruments Methods Phys. Res. Sect. A Accel. Spectrometers, Detect. Assoc. Equip.* **702** (2013) 83-7.

[43] Zaidi H., Ojha N., Morich M., Griesmer J., Hu Z., Maniawski P., Ratib O., Izquierdo-Garcia D., Fayad Z. A. and Shao L., *Design and performance evaluation of a whole-body Ingenuity TF PET–MRI system*, *Phys. Med. Biol.* **56** (2011) 3091–106.

[44] Slomka P. J., Pan T. and Germano G., *Recent developments in silicon avalanche photodiodes*, *Measurement* **3** (1985) 146-52.

[45] McIntyre R. J., *Recent Advances and Future Progress in PET Instrumentation*, *Semin. Nucl. Med.* **46** (2016) 5-19.

[46] Hsu D. F. C., Ilan E., Peterson W. T., Uribe J., Lubberink M. and Levin C. S., *Studies of a Next-Generation Silicon-Photomultiplier–Based Time-of-Flight PET/CT System*, *J. Nucl. Med.* **58** (2017) 1511–8.

[47] Wagatsuma K., Miwa K., Sakata M., Oda K., Ono H., Kameyama M., Toyohara J. and Ishii K., *Comparison between new-generation SiPM-based and conventional PMT-based TOF-PET/CT*, *Phys. Medica* **42** (2017) 203-10.

[48] Karp J. S., Viswanath V., Geagan M. J., Muehllehner G., Pantel A. R., Parma M. J., Perkins A. E., Schmall J. P., Werner M. E. and Daube-Witherspoon M. E., *PennPET Explorer: Design and Preliminary Performance of a Whole-Body*, *Imager J. Nucl. Med.* **61** (2020) 136-43.

[49] Spencer B. A., Berg E., Schmall J. P., Omidvari N., Leung E. K., Abdelhafez Y. G., Tang S., Deng Z., Dong Y., Lv Y., Bao J., Liu W., Li H., Jones T., Badawi R. D. and Cherry S. R., *Performance Evaluation of the uEXPLORER Total-Body PET/CT Scanner Based on NEMA NU 2-2018 with Additional Tests to Characterize PET Scanners with a Long Axial Field of View*, *J. Nucl. Med.* **62** (2021) 861–70.

[50] Prenosil G. A., Sari H., Fürstner M., Afshar-Oromieh A., Shi K., Rominger A. and Hentschel M.,

Performance Characteristics of the Biograph Vision Quadra PET/CT System with a Long Axial Field of View Using the NEMA NU 2-2018 Standard, *J. Nucl. Med.* **63** (2022) 476-84.

[51] Liu Z., Niu M., Kuang Z., Ren N., Wu S., Cong L., Wang X., Sang Z., Williams C. and Yang Y., *High resolution detectors for whole-body PET scanners by using dual-ended readout*, *EJNMMI Phys.* **9** (2022) 29.

[52] Grant A. M., Deller T. W., Khalighi M. M., Maramraju S. H., Delso G. and Levin C. S., *NEMA NU 2-2012 performance studies for the SiPM-based ToF-PET component of the GE SIGNA PET/MR system*, *Med. Phys.* **43** (2016) 2334–43.

[53] Son J-W., Kim K. Y., Park J. Y., Kim K., Lee Y-S., Ko G. B. and Lee J. S., *SimPET: a Preclinical PET Insert for Simultaneous PET/MR Imaging*, *Mol. Imaging Biol.* **22** (2020) 1208–17.

[54] Kang H. G., Tashima H., Nishikido F., Akamatsu G., Wakizaka H., Higuchi M. and Yamaya T., *Initial results of a mouse brain PET insert with a staggered 3-layer DOI detector*, *Phys. Med. Biol.* **2** (2021) 0-31.

[55] Nishikido F., Obata T., Suga M., Iwao Y., Tashima H., Yoshida E., Akram M. S. H., Yamaya T., *Axial scalable add-on PET/MR prototype based on four-layer DOI detectors integrated with a RF coil*, *Nuclear Instruments and Methods in Physics Research Section A: Accelerators, Spectrometers, Detectors and Associated Equipment* **1040** (2022) 167239.

[56] Khateri P., Lustermann W., Ritzer C., Tsoumpas C. and Dissertori G., *NEMA characterization of the SAFIR prototype PET insert*, *EJNMMI Phys.* **9** (2022) 42.

[57] Delso G., Furst S., Jakoby B., Ladebeck R., Ganter C., Nekolla S., Schwaiger M. and Ziegler S. I., *Performance Measurements of the Siemens mMR Integrated Whole-Body PET/MR Scanner*, *Journal of Nuclear Medicine* **12** (2011) 1914–1922.

[58] Disselhorst J. A., Newport D. F., Schmid A. M., Schmidt F. P., Parl C., Liu C-C., Pichler B. J. and Mannheim J. G., *NEMA NU 4-2008 performance evaluation and MR compatibility tests of an APD-based small animal PET-insert for simultaneous PET/MR imaging*, *Phys. Med. Biol.* **67** (2022) 045015.

[59] Anger H. O., *Scintillation Camera and Multiplane Tomographic Scanner*, *Lawrence Berkeley National Laboratory* (1969).

[60] van Sluis J., de Jong J., Schaar J., Noordzij W., van Snick P., Dierckx R., Borra R., Willemsen A. and Boellaard R., *Performance Characteristics of the Digital Biograph Vision PET/CT System*, *J. Nucl. Med.* **60** (2019) 1031–6.

[61] Conti M., *Focus on time-of-flight PET: the benefits of improved time resolution*, *Eur. J. Nucl. Med. Mol. Imaging* **38** (2011) 1147–57.

[62] Catana, C., Guimaraes, A. R., Rosen, B. R., *PET and MR imaging: the odd couple or a match made in heaven?*, *J Nucl Med* **54(5)** (2013) 815-824.

[63] Cabello, J., Ziegler, S. I., *Advances in PET/MR instrumentation and image reconstruction*, *The British journal of radiology* **91(1081)** (2018) 20160363.

[64] Pichler, B., Lorenz, E., Mirzoyan, R., Pimpl, W., Roder, F., Schwaiger, M., Ziegler, S. I., *Performance test of a LSO-APD PET module in a 9.4 Tesla magnet*, *1997 IEEE Nuclear Science Symposium Conference Record* **2** (1997) 1237-1239.

[65] Garlick P. B., Marsden, P. K., Cave, A. C., Parkes, H. G., Slates, R., Shao, Y., Silverman, R. W., Cherry, S. R., *PET and NMR dual acquisition (PANDA): applications to isolated, perfused rat hearts*, *NMRBiomed* **10(3)** (1997) 138–142.

[66] Cherry, S. R., *Multimodality in vivo imaging systems: Twice the power or double the trouble?*, *Annual Review of Biomedical Engineering* **8(1)** (2006) 35e62.

[67] Catana, C., Wu, Y., Judenhofer, M. S., Qi, J., Pichler, B. J., Cherry, S. R., *Simultaneous acquisition of multislice PET and MR images: initial results with a MR-compatible PET scanner*, *J Nucl Med* **47(12)** (2006) 1968-1976.

[68] Judenhofer, M. S., Wehrl, H. F., Newport, D. F., Catana, C., Siegel, S. B., Becker, M., ..., Pichler, B. J., *Simultaneous PET-MRI: a new approach for functional and morphological imaging*, *Nature medicine* **14(4)** (2008) 459-465.

[69] Catana, C., Procissi, D., Wu, Y., Judenhofer, M. S., Qi, J., Pichler, B. J., ..., Cherry, S. R., *Simultaneous in vivo positron emission tomography and magnetic resonance imaging*, *Proceedings of the National Academy of Sciences* **105(10)** (2008) 3705-3710.

[70] Wu, Y., Catana, C., Farrell, R., Dokhale, P. A., Shah, K. S., Qi, J., Cherry, S. R., *PET performance evaluation of an MR-compatible PET insert*, *IEEE transactions on nuclear science* **56(3)** (2009) 574-580.

[71] Schmand, M., Burbar, Z, Corbeil, J., Zhang, N., Michael, C., Byars, L., ..., Heiss, W, *BrainPET: First human tomograph for simultaneous (functional) PET and MR imaging*, *J Nucl Med* **48(suppl. 2)** (2007) 310P.

[72] Herzog, H., Langen, K. J., Weirich, C., Rota Kops, E., Kaffanke, J., Tellmann, L., Scheins, J., Neuner, I., Stoffels, G., Fischer, K., Caldeira, L., Coenen, H. H., Shah, N. J., *High resolution BrainPET combined with simultaneous MRI*, *Nuklearmedizin* **50(2)** (2011) 74-82.

[73] Luna, A., Vilanova, J. C, Hygino de la Cruz Jr, L. C., Rossi, S. E., *Functional Imaging in Oncology: Biophysical Basis and Technical Approaches*, Springer Science & Business Media (2013).

[74] Zaidi, H., *PET/MR: Advances in Instrumentation and Quantitative Procedures, An Issue of PET Clinics*, Elsevier Health Sciences (2016).

[75] Herzog, H., Lerche, C., *Advances in Clinical PET/MR Instrumentation*, *PET Clin* **11** (2011) 95-103.

[76] Roncali, E. & Cherry, S.R., *Application of silicon photomultipliers to positron emission tomography*, *Annals of Biomedical Engineering* **39(4)** (2011) 1358-1377.

[77] Levin, C. S., Maramraju, S. H., Khalighi, M. M, Deller, T. W., Delso, G., Jansen, F., *Design features and mutual compatibility studies of the timeof-flight PET capable GE SIGNA PET/MR system*, *IEEE Trans Med Imaging* **35(8)** (2016) 1907-1914.

[78] Zaidi H., Hasegawa B., *Determination of the attenuation map in emission tomography*, *J Nucl Med* **44** (2003) 291-315.

[79] Zaidi H. and Montandon M. L., *Scatter compensation techniques in PET*, *PET Clin* **2** (2007) 219-234.

[80] Martinez-Möller, A., Nekolla, S. G., *Attenuation correction for PET/MR: problems, novel approaches and practical solutions*, *Med Phys* **22** (2012) 299-310.

[81] Torrado-Carvajal, A., *Importance of attenuation correction in PET/MR image quantification: Methods and applications*, *Revista Española de Medicina Nuclear e Imagen Molecular (English Edition)* **39(3)** (2020) 163-168.

[82] Huang, S.C., Hoffman, E. J., Phelps, M. E., Kuhl, D. E., *Quantitation in positron emission computed tomography: 2. Effects of inaccurate attenuation correction*, *Journal of Computer Assisted Tomography* **3(6)** (1979) 804-814.

[83] Wagenknecht, G., Kaiser, H-J., Mottaghy, F. M., Herzog, H., *MRI for attenuation correction in PET: methods and challenges*, *Magnetic resonance materials in physics, biology and medicine* **26(1)** (2013) 99-113.

[84] Burger, C., Goerres, G., Schoenes, S., Buck, A., Lonn, A., Von Schulthess, G., *PET attenuation coefficients from CT images: experimental evaluation of the transformation of CT into PET 511-keV attenuation coefficients*, *Eur J Nucl Med Mol Imaging* **29(7)** (2002) 922-927.

[85] Andersen, F. L., Ladefoged, C. N., Beyer, T., Keller, S. H., Hansen, A. E., Højgaard, L., Kjær, A., Law, I., Holm, S., *Combined PET/MR imaging in neurology: MR-based attenuation correction implies a strong spatial bias when ignoring bone*, *Neuroimage* **84** (2014) 206-216.

[86] Hofmann, M., Pichler, B., Schölkopf, B., Beyer, T., *Towards quantitative PET/MR:a review of MR-based attenuation correction techniques*, *Eur J Nucl Med Mol Imaging* **36** (2009) S93-104.

[87] Teuho, J., Torrado-Carvajal, A., Herzog, H., Anazodo, U., Klén, R., Iida, H., & Teräs, M., *Magnetic resonance-based attenuation correction and scatter correction in neurological positron emission tomography/magnetic resonance imaging—current status with emerging applications*, *Frontiers in Physics* **7** (2020) 243.

[88] Martinez-Möller, A., Souvatzoglou, M., Delso, G., Bundschuh, RA., Chefd'hotel, C.,Ziegler, S. I., Navab, N., Schwaiger, M., Nekolla, S. G., *Tissue classification as a potential approach for attenuation correction in whole-body PET/MR: evaluation with PET/CT data*, *J Nucl Med* **50** (2009) 520-526.

[89] Torrado-Carvajal, A., Herraiz, J. L., Hernandez-Tamames, J. A., San Jose-Estepar, R., Eryaman, Y., Rozenholc, Y., et al, *Multi-atlas and label fusion approach for patient-specific MRI based skull estimation*, *Magn Reson Med* **75** (2016) 1797-1807.

[90] Izquierdo-Garcia, D., Hansen, A. E., Förster, S., Benoit, D., Schachoff, S., Fürst S., et al. , *An SPM8-based approach for attenuation correction combining segmentation and nonrigid template formation: application tosimultaneous PET/MR brain imaging*, *J Nucl Med* **55** (2014) 1825-1830.

[91] Torrado-Carvajal, A., Herraiz, J. L., Alcain, E., Montemayor, A.S., Garcia-Cañamaque, L., Hernandez-Tamames, J. A., et al, *Fast patch-based pseudo-CT synthesis from T1-weighted MR images for PET/MR attenuation correction in brain studies*, *J NuclMed* **57** (2016) 136-143.

[92] Hofmann, M., Steinke, F., Scheel, V., Charpiat, G., Farquhar, J., Aschoff, P., et al, *MRI-based attenuation correction for PET/MR: a novel approach combining pattern recognition and atlas registration*, *J Nucl Med* **49** (2008) 1875-1883.

[93] Burgos, N., Cardoso, M. J., Thielemans, K., Modat, M., Pedemonte, S., Dickson, J., et al., *Attenuation correction synthesis for hybrid PET-MR scanners: application to brain studies*, *IEEE Trans Med Imaging* **33** (2014) 2232-2241.

[94] Ribeiro, A., Mops, E., Herzog, H., Almeida, P., *Hybrid approach for attenuation correction in PET/MR scanners*, *Nucl Instrum Meth A* **734** (2014) 166-170.

[95] Martinez-Girones, P. M., Vera-Olmos, J., Gil-Correa, M., Ramos, A., Garcia-Cañamaque, L., Izquierdo-Garcia, D., ..., Torrado-Carvajal, A, *Franken-CT: Head and Neck MR-Based Pseudo-CT Synthesis Using Diverse Anatomical Overlapping MR-CT Scans*, *Applied Sciences* **11(8)** (2021) 3508.

[96] Ladefoged, C. N., Law, I., Anazodo, U., Lawrence, K. S., Izquierdo-Garcia, D., Catana, C., et al, *A multi-centre evaluation of eleven clinically feasible brain PET/MR attenuation correction techniques using a large cohort of patients*, *Neuroimage* **147** (2017) 346-359.

[97] Izquierdo-Garcia, D., & Catana, C, *MR imaging–guided attenuation correction of PET data in PET/MR imaging*, *PET clinics* **11(2)** (2016) 129-149.

[98] Catana, C, *Attenuation correction for human PET/MR studies*, *Phys Med Biol* **65(23)** (2020) 23TR02.

[99] Leynes, A. P., Yang, J., Shanbhag, D. D., Kaushik, S. S., Seo, Y., Hope, T. A., et al, *Hybrid ZTE/Dixon MR-based attenuation correction for quantitative uptake estimation of pelvic lesions in PET/MR*, *Med Phys* **44** (2017) 902-913.

[100] Leynes, A. P., Yang, J., Wiesinger, F., Kaushik, S. S., Shanbhag, D. D., Seo, Y., et al, *Zero echo-time and dixon deep pseudoCT (ZeDD-CT): Direct generation of pseudoCT Images for pelvic PET/MR attenuation correction using deep convolutional neural networks with multi-parametric MRI*, *J Nucl Med* **59** (2018) 852-858.

[101] Torrado-Carvajal, A., Vera-Olmos, J., Izquierdo-Garcia, D., Catalano, O. A., Morales, M. A., Margolin, J., et al, *Dixon-VIBE Deep Learning (DIVIDE) pseudo-CT synthesis for pelvis PET/MR attenuation correction*, *J Nucl Med* **60** (2019) 429-435.

[102] Pozaruk, A., Pawar, K., Li, S., Carey, A., Cheng, J., Sudarshan, V. P., Cholewa, M., Grummet, J., Chen, Z., & Egan, G., *Augmented deep learning model for improved quantitative accuracy of MR-based PET attenuation correction in PSMA PET-MRI prostate imaging*, *Eur J Nucl Med Mol Imaging* **48(1)** (2021) 9-20.

[103] Sari, H., Reaungamornrat, J., Catalano, O. A., Vera-Olmos, J., Izquierdo-Garcia, D., Morales, M. A., Torrado-Carvajal, A., Ng, T. S. C., Malpica, N., Kamen, A., Catana, C., *Evaluation of Deep Learning-Based Approaches to Segment Bowel Air Pockets and Generate Pelvic Attenuation Maps from CAIPIRINHA-Accelerated Dixon MR Images*, *J Nucl Med* **63(3)** (2022) 468-475.

[104] Beyer, T., Weigert, M., Quick, H. H., Pietrzyk, U., Vogt, F., Palm, C., ..., Bockisch, A, *MR-based attenuation correction for torso-PET/MR imaging: pitfalls in mapping MR to CT data*, *Eur J Nucl Med Mol Imaging* **35(6)** (2008) 1142-1146.

[105] Marshall, H. R., Prato, F. S., Deans, L., Théberge, J., Thompson, R. T., Stodilka, R. Z., *Variable lung density consideration in attenuation correction of whole-body PET/MR*, *J Nucl Med* **53(6)** (2012) 977-984.

[106] Lau, J. M., Laforest, R., Sotoudeh, H., Nie, X., Sharma, S., McConathy, J., ..., Woodard, P. K., *Evaluation of attenuation correction in cardiac PET using PET/MR*, *Journal of Nuclear Cardiology* **24(3)** (2017) 839-846.

[107] Lassen, M. L., Rasul, S., Beitzke, D., Stelzmüller, M. E., Cal-Gonzalez, J., Hacker, M., & Beyer, T., *Assessment of attenuation correction for myocardial PET imaging using combined PET/MR*, *Journal of Nuclear Cardiology* **26(4)** (2019) 1107-1118.

[108] Masuda, A., Nemoto, A., & Takeishi, Y., *Technical aspects of cardiac PET/MR*, *Journal of Nuclear Cardiology* **25(3)** (2018) 1023-1028.

[109] Nuyts, J., Bal, G., Kehren, F., Fenchel, M., Michel, C., Watson, C., *Completion of a truncated attenuation image from the attenuated PET emission data*, *IEEE Trans Med Imaging* **32** (2013) 237-246.

[110] Fuin, N., Pedemonte, S., Catalano, O. A., Izquierdo-Garcia, D., Soricelli, A., Salvatore, M., ..., Catana, C., *PET/MR in the presence of metal implants: completion of the attenuation map from PET emission data*, *J Nucl Med* **58(5)** (2017) 840-845.

[111] Schramm, G., & Ladefoged, C. N., *Metal artifact correction strategies in MRI-based attenuation correction in PET/MR*, *BJR Open* **1** (2019) 20190033.

[112] Afshar-Oromieh A, Wolf M, Haberkorn U, Kachelrieß M, Gnirs R, Kopka K, Schlemmer H-P and

Freitag M T, *Effects of arm truncation on the appearance of the halo artifact in 68Ga-PSMA-11 (HBED-CC) PET/MR*, *Eur. J. Nucl. Med. Mol. Imaging* **44** (2017) 1636–46.

[113] Heußer T, Mann P, Rank C M, Schäfer M, Dimitrakopoulou-Strauss A, Schlemmer H-P, Hadaschik B A, Kopka K, Bachert P, Kachelrieß M and Freitag M T, *Investigation of the halo-artifact in 68Ga-PSMA-11-PET/MR*, *ed B Thierry PLoS One* **12** (2017) e0183329.

[114] Lindemann M E, Guberina N, Wetter A, Fendler W P, Jakoby B and Quick H H, *Improving 68 Ga-PSMA PET/MR of the Prostate with Unrenormalized Absolute Scatter Correction*, *J. Nucl. Med.* **60** (2019) 1642–8.

[115] Zaidi, H., Koral, K. F., *Scatter modelling and compensation in emission tomography*, *Eur J Nucl Med Mol Imaging* **31** (2004) 761-782.

[116] Castiglioni I, Cremonesi O, Gilardi M C, Bettinardi V, Rizzo G, Savi A, Bellotti E and Fazio F, *Scatter correction techniques in 3D PET: a Monte Carlo evaluation*, *IEEE Trans. Nucl. Sci.* **46** (1999) 2053–8.

[117] Popescu L M, Lewitt R M, Matej S and Karp J S, *PET energy-based scatter estimation and image reconstruction with energy-dependent corrections*, *Phys. Med. Biol.* **51** (2006) 2919–37.

[118] Álvarez-Gómez J M, Santos-Blasco J, Moliner Martínez L and Rodríguez-Álvarez M J, *Fast Energy Dependent Scatter Correction for List-Mode PET Data*, *J. Imaging* **7** (2021) 199.

[119] Watson C C, Newport D and Casey M E, *A Single Scatter Simulation Technique for Scatter Correction in 3D PET*, *Three-Dimensional Image Reconstruction in Radiology and Nuclear Medicine* (1996) 255–68.

[120] Ollinger J M, *Model-based scatter correction for fully 3D PET*, *Phys. Med. Biol.* **41** (1996) 153–76.

[121] Watson C C, *New, faster, image-based scatter correction for 3D PET*, *IEEE Trans. Nucl. Sci.* **47** (2000) 1587–94.

[122] Werling A, Bublitz O, Doll J, Adam L-E and Brix G, *Fast implementation of the single scatter simulation algorithm and its use in iterative image reconstruction of PET data*, *Phys. Med. Biol.* **47** (2002) 310.

[123] Thielemans K, Manjeshwar R M, Tsoumpas C and Jansen F P, *A new algorithm for scaling of PET scatter estimates using all coincidence events*, *2007 IEEE Nuclear Science Symposium Conference Record* **5** (2007) 3586–90.

[124] Ma B, Xu H, Lenz M, Pietrzyk U, Shah N J, Gaens M, Caldeira L, Bert J, Lohmann P, Tellmann L, Lerche C, Scheins J and Rota Kops E, *Scatter Correction Based on GPU-Accelerated Full Monte Carlo Simulation for Brain PET/MR*, *IEEE Trans. Med. Imaging* **39** (2020) 140–51.

[125] Polycarpou I, Thielemans K, Manjeshwar R, Aguiar P, Marsden P K and Tsoumpas C, *Comparative evaluation of scatter correction in 3D PET using different scatter-level approximations*, *Ann. Nucl. Med.* **25** (2011) 643–9.

[126] Watson C C, Hu J and Zhou C, *Double Scatter Simulation for More Accurate Image Reconstruction in Positron Emission Tomography*, *IEEE Trans. Radiat. Plasma Med. Sci.* **4** (2020) 570–84.

[127] Kyung Sang Kim, Young Don Son, Zang Hee Cho, Jong Beom Ra and Jong Chul Ye, *Ultra-Fast Hybrid CPU–GPU Multiple Scatter Simulation for 3-D PET*, *IEEE J. Biomed. Heal. Informatics* **18** (2014) 148–56.

[128] Holdsworth C H, Levin C S, Farquhar T H, Dahlbom M and Hoffman E J, *Investigation of*

accelerated Monte Carlo techniques for PET simulation and 3D PET scatter correction, *IEEE Trans. Nucl. Sci.* **48** (2001) 74–81.

[129] Scheins J J, Lenz M, Pietrzyk U, Shah N J and Lerche C, *High-throughput, accurate Monte Carlo simulation on CPU hardware for PET applications*, *Phys. Med. Biol.* **66** (2021) 185001.

[130] Ye J, Song X and Hu Z, *Scatter correction with combined single-scatter simulation and Monte Carlo simulation for 3D PET*, *2014 IEEE Nuclear Science Symposium and Medical Imaging Conference (NSS/MIC) (IEEE)* (2014) 1-3.

[131] Pönisch F, Enghardt W and Lauckner K, *Attenuation and scatter correction for in-beam positron emission tomography monitoring of tumour irradiations with heavy ions*, *Phys. Med. Biol.* **48** (2003) 2419–36.

[132] Qian H, Rui X and Ahn S, *Deep Learning Models for PET Scatter Estimations*, *2017 IEEE Nuclear Science Symposium and Medical Imaging Conference (NSS/MIC)* (2017) 1-5.

[133] Berker Y, Maier J and Kachelries M, *Deep Scatter Estimation in PET: Fast Scatter Correction Using a Convolutional Neural Network*, *2018 IEEE Nuclear Science Symposium and Medical Imaging Conference Proceedings (NSS/MIC)* (2018) 1-5.

[134] Laurrent B, Merlin T, Bousse A and Visvikis D, *Deep learning based scatter correction for PET imaging*, *2020 IEEE Nuclear Science Symposium and Medical Imaging Conference* (2020).

[135] Xiang H, Lim H, Fessler J A and Dewaraja Y K, *A deep neural network for fast and accurate scatter estimation in quantitative SPECT/CT under challenging scatter conditions*, *Eur. J. Nucl. Med. Mol. Imaging* **47** (2020) 2956–67.

[136] Prats J, Larroza A, Oliver S and Rodriguez-Alvarez M J, *PET scatter correction using machine learning techniques*, *2019 IEEE Nuclear Science Symposium and Medical Imaging Conference (NSS/MIC)* (2019) 1-3.

[137] Yang J, Park D, Gullberg G T and Seo Y, *Joint correction of attenuation and scatter in image space using deep convolutional neural networks for dedicated brain 18 F-FDG PET*, *Phys. Med. Biol.* **64** (2019) 075019.

[138] Shiri I, Arabi H, Geramifar P, Hajianfar G, Ghafarian P, Rahmim A, Ay M R and Zaidi H, *Deep-JASC: joint attenuation and scatter correction in whole-body 18F-FDG PET using a deep residual network*, *Eur. J. Nucl. Med. Mol. Imaging* **47** (2020) 2533–48.

[139] Arabi H, Bortolin K, Ginovart N, Garibotto V and Zaidi H, *Deep learning-guided joint attenuation and scatter correction in multitracer neuroimaging studies*, *Hum. Brain Mapp.* **41** (2020) 3667–79.

[140] Yang J, Sohn J H, Behr S C, Gullberg G T and Seo Y, *CT-less Direct Correction of Attenuation and Scatter in the Image Space Using Deep Learning for Whole-Body FDG PET: Potential Benefits and Pitfalls*, *Radiol. Artif. Intell.* **3** (2021) e200137.

[141] Spangler-Bickell, M. G., Hurley, S. A., Pirasteh, A., Perlman, S. B., Deller, T., McMillan, A. B., *Evaluation of Data-Driven Rigid Motion Correction in Clinical Brain PET Imaging*, *Journal of Nuclear Medicine October* **63(10)** (2022) 1604-1610.

[142] Rahmim A, Rousset O, Zaidi H., *Strategies for motion tracking and correction in PET*, *PET Clinics* **2** (2007) 251-266.

[143] Zhou, V. W., Kyme, A. Z., Meikle, S. R., Fulton, R., *A scheme for PET data normalization in event-based motion correction*, *Phys Med Biol* **54** (2009) 5321–5339.

[144] Catana, C., Benner, T., van der Kouwe, A., Byars, L., Hamm, M., Chonde, D. B., ..., Sorensen, A. G., *MRI-assisted PET motion correction for neurologic studies in an integrated MR-PET scanner*, *J Nuc Med* **52(1)** (2011) 154-161.

[145] Keller, S. H., Hansen, C., Hansen, C., Andersen, F. L., Ladefoged, C., Svarer, C., ..., Hansen, A. E., *Motion correction in simultaneous PET/MR brain imaging using sparsely sampled MR navigators: a clinically feasible tool*, *Eur J Nucl Med Mol Imaging* **2(1)** (2015) 1-7.

[146] Levine, M. A., Mandeville, J. B., Calabro, F., et al, *Assessment of motion and model bias on the detection of dopamine response to behavioral challenge*, *Journal of Cerebral Blood Flow & Metabolism* **42(7)** (2022) 1309-1321.

[147] Chun, S. Y., Reese, T. G., Ouyang, J., Guerin, B., Catana, C., Zhu, X., ..., El Fakhri, G., *MRI-based nonrigid motion correction in simultaneous PET/MR*, *J Nuc Med* **53(8)** (2022) 1284-1291.

[148] Manber, R., Thielemans, K., Hutton, B., Barnes, A., Ourselin, S., Arridge, S., et al, *Practical PET respiratory motion correction in clinical PET/ MR*, *J Nuc Med* **56** (2015) 890-896.

[149] Küstner, T., Schwartz, M., Martirosian, P., Gatidis, S., Seith, F., Gilliam, C., et al, *MR-based respiratory and cardiac motion correction for PET imaging*, *Med Image Anal* **42** (2017) 1229-144.

[150] Kolbitsch, C., Ahlman, M. A., Davies-Venn, C., Evers, R., Hansen, M., Peressutti, D., et al, *Cardiac and respiratory motion correction for simultaneous cardiac PET/MR*, *J Nuc Med* **58** (2017) 846-852.

[151] Kolbitsch, C., Prieto, C., Tsoumpas, C., & Schaeffter, T., *A 3D MR-acquisition scheme for nonrigid bulk motion correction in simultaneous PET-MR*, *Med Phys* **41(8Part1)** (2014) 082304.

[152] Munoz, C., Kunze, K. P., Neji, R., Vitadello, T., Rischpler, C., Botnar, R. M., ..., Prieto, C., *Motion-corrected whole-heart PET-MR for the simultaneous visualisation of coronary artery integrity and myocardial viability: an initial clinical validation*, *Eur J Nucl Med Mol Imaging* **45(11)** (2018) 1975-1986.

[153] Morales, M. A., Izquierdo-Garcia, D., Aganj, I., Kalpathy-Cramer, J., Rosen, B. R., & Catana, C., *Implementation and validation of a three-dimensional cardiac motion estimation network*, *Radiology: Artificial Intelligence* **1(4)** (2019) e180080.

[154] Qi J. and Leahy R. M., *Iterative reconstruction techniques in emission computed tomography*, *Phys. Med. Biol.* **51** (2006) R541–78.

[155] Tong S., Alessio A. M. and Kinahan P. E., *Image reconstruction for PET/CT scanners: past achievements and future challenges*, *Imaging Med.* **2** (2010) 529–45.

[156] Iriarte A., Marabini R., Matej S., Sorzano C. O. S. and Lewitt R. M., *System models for PET statistical iterative reconstruction: A review*, *Comput. Med. Imaging Graph.* **48** (2016) 30-48.

[157] Gong K., Kim K., Cui J., Wu D. and Li Q., *The Evolution of Image Reconstruction in PET: From Filtered Back-Projection to Artificial Intelligence PET*, *Clin.* **16** (2021) 533–42.

[158] Reader A. J., Corda G., Mehranian A., Costa-Luis C. da, Ellis S. and Schnabel J. A., *Deep Learning for PET Image Reconstruction*, *IEEE Trans. Radiat. Plasma Med. Sci.* **5** (2021) 1-25.

[159] Arabi H., AkhavanAllaf A., Sanaat A., Shiri I. and Zaidi H., *The promise of artificial intelligence and deep learning in PET and SPECT imaging*, *Phys. Medica* **83** (2021) 122–37.

[160] Reader A. J. and Schramm G., *Artificial Intelligence for PET Image Reconstruction*, *J. Nucl. Med.* **62** (2021) 1330–3.

[161] Easton R. L., *Fourier Methods in Imaging*, *Chichester, UK: John Wiley & Sons, Ltd* (2010).

[162] Cherry S., Sorenson J and Phelps M, *Physics in Nuclear Medicine*, *Elsevier* (2012).

[163] Alessio A. and Kinahan P. E., *PET Image Reconstruction*, *Nuclear Medicine (Elsevier)* (2006).

[164] Kinahan P. E. and Rogers J. G., *Analytic 3D image reconstruction using all detected events*, *IEEE Transactions on Nuclear Science* **36(1)** (1989) 964-968.

[165] López-Montes A., Galve P., Udias J. M., Cal-González J., Vaquero J. J., Desco M. and Herraiz J. L., *Real-Time 3D PET Image with Pseudoinverse Reconstruction*, *Appl. Sci.* **10** (2020) 2829.

[166] Lopez Montes A., Galve P., Udias J. M. and Herraiz J. L., *Application of the pseudoinverse for real-time 3D PET image reconstruction*, *15th International Meeting on Fully Three-Dimensional Image Reconstruction in Radiology and Nuclear Medicine ed S Matej and S D Metzler (SPIE)* (2019) 74.

[167] Herraiz J. L., Espana S., Vicente E., Vaquero J. J., Desco M. and Udias J. M., *Optimal and Robust PET Data Sinogram Restoration Based on the Response of the System*, *2006 IEEE Nuclear Science Symposium Conference Record* **6** (2006) 3404–7.

[168] Herraiz J. L., Espana S., Vicente E., Herranz E., Desco M., Vaquero J. J. and Udias J., *Frequency selective signal extrapolation for compensation of missing data in sinograms*, *2008 IEEE Nuclear Science Symposium Conference Record* (2008) 4299–302.

[169] Daube-Witherspoon M. E. and Muehllehner G., *Treatment of axial data in three-dimensional PET*, *J. Nucl. Med.* **28** (1987) 1717–24.

[170] Defrise M., Kinahan P. E., Townsend D. W., Michel C., Sibomana M. and Newport D. F., *Exact and approximate rebinning algorithms for 3-D PET data*, *IEEE Trans. Med. Imaging* **16** (1997) 145–58.

[171] Liu X., Defrise M., Michel C., Sibomana M., Comtat C., Kinahan P. and Townsend D., *Exact rebinning methods for three-dimensional PET*, *IEEE Transactions on Medical Imaging* **18(8)** (1999) 657–664.

[172] Ben Bouallegue F., Crouzet J-F., Comtat C., Fourcade M., Mohammadi B. and Mariano-Goulart D., *Exact and Approximate Fourier Rebinning Algorithms for the Solution of the Data Truncation Problem in 3-D PET*, *IEEE Trans. Med. Imaging* **26** (2007) 1001-9.

[173] National Electrical Manufacturers Association 2007, *NEMA Standards Publication NU 2-2007 Performance Measurements of Positron Emission Tomographs*, *Rosslyn, VA: National Electrical Manufacturers Association* (2007).

[174] National Electrical Manufacturers Association 2008, *NEMA Standards Publication NU 4-2008 Performance Measurements of Small Animal Positron Emission Tomographs*, *Rosslyn, VA: National Electrical Manufacturers Association* (2007).

[175] Defrise M. and Kinahan P., *Data Acquisition and Image Reconstruction for 3D PET The Theory and Practice of 3D PET*, *ed B Bendriem and D W Townsend (Kluwer Academic Publisher)* (1998) 11-53.

[176] Comtat C., Bataille F., Michel C., Jones J. P., Sibomana M., Janeiro L. and Trebossen R., *OSEM-3D Reconstruction Strategies for the ECAT HRRT*, *IEEE Symposium Conference Record Nuclear Science 2004* **6** (2004) 3492–6.

[177] Zaidi H. and Karakatsanis N., *Towards enhanced PET quantification in clinical oncology*, *Br. J. Radiol.* **91** (2018) 20170508.

[178] Siddon R. L., *Fast calculation of the exact radiological path for a three-dimensional CT array*, *Med. Phys.* **12** (1985) 252–5.

[179] Zeng G. L., Gullberg G. T., Tsui B. M. W. and Terry J. A., *Three-dimensional iterative*

reconstruction algorithms with attenuation and geometric point response correction, *IEEE Trans. Nucl. Sci.* **38** (1991) 693–702.

[180] Lougovski A., Hofheinz F., Maus J., Schramm G., Will E. and Hoff J. V. D., *A volume of intersection approach for on-the-fly system matrix calculation in 3D PET image reconstruction*, *Phys. Med. Biol.* **59** (2014) 561–77.

[181] Markiewicz P. J., Thielemans K., Ehrhardt M. J., Jiao J., Burgos N., Atkinson D., Arridge S. R., Hutton B. F. and Ourselin S., *High throughput CUDA implementation of accurate geometric modelling for iterative reconstruction of PET data*, *2014 IEEE Nuclear Science Symposium and Medical Imaging Conference (NSS/MIC)* (2014) 1–4.

[182] Huesman R. H., Klein G. J., Moses W. W., Qi J., Reutter B. W. and Virador P. R. G., *List-mode maximum-likelihood reconstruction applied to positron emission mammography (PEM) with irregular sampling*, *IEEE Trans. Med. Imaging* **19** (2000) 532–7.

[183] Moehrs S., Defrise M., Belcari N., Guerra A. D., Bartoli A., Fabbri S. and Zanetti G., *Multi-ray-based system matrix generation for 3D PET reconstruction*, *Phys. Med. Biol.* **53** (2008) 6925–45.

[184] Pratx G., Chinn G., Olcott P. D. and Levin C. S., *Fast, Accurate and Shift-Varying Line Projections for Iterative Reconstruction Using the GPU*, *IEEE Trans. Med. Imaging* **28** (2009) 435–45.

[185] Li K., Safavi-Naeini M., Franklin D. R., Han Z., Rosenfeld A. B., Hutton B. and Lerch M. L. F., *A new virtual ring-based system matrix generator for iterative image reconstruction in high resolution small volume PET systems*, *Phys. Med. Biol.* **60** (2015) 6949–73.

[186] Reader A. J., Julyan P. J., Williams H., Hastings D. L. and Zweit J., *EM algorithm system modeling by image-space techniques for PET reconstruction*, *IEEE Trans. Nucl. Sci.* **50** (2003) 1392–7.

[187] Rogasch J. M. M., Boellaard R., Pike L., Borchmann P., Johnson P., Wolf J., Barrington S. F. and Kobe C., *Moving the goalposts while scoring—the dilemma posed by new PET technologies*, *Eur. J. Nucl. Med. Mol.* **48** (2021) 2696–710.

[188] Gillam J. E. and Rafecas M., *Monte-Carlo simulations and image reconstruction for novel imaging scenarios in emission tomography*, *Nucl. Instruments Methods Phys. Res. Sect. A Accel. Spectrometers, Detect. Assoc. Equip.* **809** (2016) 76–88.

[189] Galve P., Udias J. M., Lopez-Montes A., Arias-Valcayo F., Vaquero J. J., Desco M. and Herraiz J. L., *Super-Iterative Image Reconstruction in PET*, *IEEE Trans. Comput. Imaging* **7** (2021) 248–57.

[190] Rapisarda E., Bettinardi V., Thielemans K. and Gilardi M. C., *Image-based point spread function implementation in a fully 3D OSEM reconstruction algorithm for PET*, *Phys. Med. Biol.* **53** (2010) 4131–51.

[191] Kotasidis F. A., Matthews J. C., Angelis G. I., Noonan P. J., Jackson A., Price P., Lionheart W. R. and Reader A. J., *Single scan parameterization of space-variant point spread functions in image space via a printed array: the impact for two PET/CT scanners*, *Phys. Med. Biol.* **56** (2011) 2917–42.

[192] Miranda A., Bertoglio D., Glorie D., Stroobants S., Staelens S. and Verhaeghe J., *Validation of a spatially variant resolution model for small animal brain PET studies*, *Biomed. Phys. Eng.* **Express 6** (2020) 045001.

[193] Alessio A. M., Kinahan P. E., Harrison R. L. and Lewellen T. K., *Measured Spatially Variant System Response for PET Image Reconstruction*, *IEEE Nuclear Science Symposium Conference Record* **4** (2005) 1986–90.

[194] Panin V. Y., Kehren F., Michel C. and Casey M., *Fully 3-D PET reconstruction with system matrix derived from point source measurements*, *IEEE Trans. Med. Imaging* **25** (2006) 907–21.

[195] Tohme M. S. and Qi J., *Iterative image reconstruction for positron emission tomography based on a detector response function estimated from point source measurements*, *Phys. Med. Biol.* **54** (2009) 3709–25.

[196] Zhou J. and Qi J., *Fast and efficient fully 3D PET image reconstruction using sparse system matrix factorization with GPU acceleration*, *Phys. Med. Biol.* **56** (2011) 6739–57.

[197] Gong K., Zhou J., Tohme M., Judenhofer M., Yang Y. and Qi J., *Sinogram Blurring Matrix Estimation From Point Sources Measurements With Rank-One Approximation for Fully 3-D PET*, *IEEE Trans. Med. Imaging* **36** (2017) 2179–88.

[198] Espana S., Herraiz J. L., Vicente E., Herranz E., Vaquero J. J., Desco M. and Udias J. M., *Improved image reconstruction in small animal PET using a priori estimates of single-pixel events*, *2007 IEEE Nuclear Science Symposium Conference Record* **5** (2007) 3876–80.

[199] Rafecas M., Mosler B., Dietz M., Pogl M., Stamatakis A., McElroy D. P. and Ziegler S. I., *Use of a Monte Carlo-based probability matrix for 3-D iterative reconstruction of MADPET-II data*, *IEEE Trans. Nucl. Sci.* **51** (2004) 2597–605.

[200] Kao C-M., Dong Y. and Xie Q., *Evaluation of 3D image reconstruction methods for a dual-head small-animal PET scanner*, *2007 IEEE Nuclear Science Symposium Conference Record* **4** (2007) 3046–50.

[201] Zhang L., Staelens S., Van Holen R., De Beenhouwer J., Verhaeghe J., Kawrakow I. and Vandenberghe S., *Fast and memory-efficient Monte Carlo-based image reconstruction for whole-body PET*, *Med. Phys.* **37** (2010) 3667–76.

[202] Southekal S., Purschke M. L., Schlyer D. J. and Vaska P., *Quantitative PET Imaging Using a Comprehensive Monte Carlo System Model*, *IEEE Trans. Nucl. Sci.* **58** (2011) 2286–95.

[203] Meng F., Wang J., Zhu S., Cheng J., Liang J. and Tian J., *Comparison of GPU reconstruction based on different symmetries for dual-head PET*, *Med. Phys.* **46** (2019) 2696–708.

[204] Zhou J. and Qi J., *Efficient fully 3D list-mode TOF PET image reconstruction using a factorized system matrix with an image domain resolution model*, *Phys. Med. Biol.* **59** (2014) 541–59.

[205] Xu H., Lenz M., Caldeira L., Ma B., Pietrzyk U., Lerche C., Shah N. J. and Scheins J., *Resolution modeling in projection space using a factorized multi-block detector response function for PET image reconstruction*, *Phys. Med. Biol.* **64** (2019) 145012.

[206] Pilleri A., Camarlinghi N., Del Guerra A., Sportelli G. and Belcari N., *A Monte Carlo detector response model for the IRIS PET preclinical scanner*, *Phys. Medica* **57** (2019) 107–14.

[207] Wei S. and Vaska P., *Evaluation of quantitative, efficient image reconstruction for VersaPET, a compact PET system*, *Med. Phys.* **47** (2020) 2852–68.

[208] Terstegge A., Weber S., Herzog H., Muller-Gartner H. W. and Halling H., *High resolution and better quantification by tube of response modelling in 3D PET reconstruction*, *1996 IEEE Nuclear Science Symposium. Conference Record* **3** (1996) 1603–7.

[209] Selivanov V. V., Picard Y., Cadorette J., Rodrigue S. and Lecomte R., *Detector response models for statistical iterative image reconstruction in high resolution PET*, *IEEE Trans. Nucl. Sci.* **47** (2000) 1168–75.

[210] Herraiz J. L., España S., Vaquero J. J., Desco M. and Udías J. M., *FIRST: Fast Iterative Reconstruction Software for (PET) tomography*, *Phys. Med. Biol.* **51** (2006) 4547–65.

[211] Meng F., Shi Y., Li C., Li L., Qin W. and Zhu S., *Hybrid model of photon propagation based on the analytical and Monte Carlo methods for a dual-head PET system*, *Phys. Med. Biol.* **66** (2021) 175008.

[212] Cal-Gonzalez J., Vaquero J. J., Herraiz J. L., Pérez-Liva M., Soto-Montenegro M. L., Peña-Zalbidea S., Desco M. and Udías J. M., *Improving PET Quantification of Small Animal [68Ga]DOTA-Labeled PET/CT Studies by Using a CT-Based Positron Range Correction*, *Mol. Imaging Biol.* **20** (2018) 584–93.

[213] Kraus R., Delso G. and Ziegler S. I., *Simulation Study of Tissue-Specific Positron Range Correction for the New Biograph mMR Whole-Body PET/MR System*, *IEEE Trans. Nucl. Sci.* **59** (2012) 1900–9.

[214] Gordon R., Bender R. and Herman G. T., *Algebraic Reconstruction Techniques (ART) for three-dimensional electron microscopy and X-ray photography*, *J. Theor. Biol.* **29** (1970) 471–81.

[215] Andersen A., *Simultaneous Algebraic Reconstruction Technique (SART): A superior implementation of the ART algorithm*, *Ultrason. Imaging* **6** (1984) 81–94.

[216] Shepp L. A. and Vardi Y., *Maximum Likelihood Reconstruction for Emission Tomography*, *IEEE Trans. Med. Imaging* **1** (1982) 113–22.

[217] Dempster A. P., Laird N. M. and Rubin D. B., *Maximum Likelihood from Incomplete Data Via the EM Algorithm*, *J. R. Stat. Soc. Ser. B* **39** (1977) 1–22.

[218] Daube-Witherspoon M. E. and Muehllehner G., *An Iterative Image Space Reconstruction Algorithm Suitable for Volume ECT*, *IEEE Trans. Med. Imaging* **5** (1986) 61–6.

[219] Hudson H. M. and Larkin R. S., *Accelerated image reconstruction using ordered subsets of projection data*, *IEEE Trans. Med. Imaging* **13** (1994) 601–9.

[220] Browne J. and de Pierro A. B., *A row-action alternative to the EM algorithm for maximizing likelihood in emission tomography*, *IEEE Trans. Med. Imaging* **15** (1996) 687–99.

[221] Reader A. J., Letourneau E. and Verhaeghe J., *Generalization of the image space reconstruction algorithm*, *IIEEE Nuclear Science Symposium Conference Record* (2011) 4233–8.

[222] Gower R. M., Schmidt M., Bach F. and Richtarik P., *Variance-Reduced Methods for Machine Learning*, *Proc. IEEE* **108** (2020) 1968–83.

[223] Ehrhardt M. J., Markiewicz P. J., Richtárik P., Schott J., Chambolle A. and Schoenlieb C-B., *Faster PET reconstruction with a stochastic primal-dual hybrid gradient method*, *Wavelets and Sparsity XVII ed Y M Lu, M Papadakis and D Van De Ville (SPIE)* (2017) 58.

[224] Ehrhardt M. J., Markiewicz P. and Schönlieb C-B., *Faster PET reconstruction with non-smooth priors by randomization and preconditioning*, *Phys. Med. Biol.* **64** (2019) 225019.

[225] Twyman R., Arridge S., Jin B., Hutton B. F., Brusaferri L. and Thielemans K., *Stochastic Variance Reduction Optimisation Algorithms Applied to Iterative PET Reconstruction*, *2020 IEEE Nuclear Science Symposium and Medical Imaging Conference (NSS/MIC)* (2020) 1-2.

[226] Kereta Ž., Twyman R., Arridge S., Thielemans K. and Jin B., *Stochastic EM methods with variance reduction for penalised PET reconstructions*, *Inverse Probl.* **37** (2021) 115006.

[227] Twyman R., Arridge S., Kereta Z., Jin B., Brusaferri L., Ahn S., Stearns C. W., Hutton B. F., Burger I. A., Kotasidis F. and Thielemans K., *An Investigation of Stochastic Variance Reduction Algorithms for Relative Difference Penalised 3D PET Image Reconstruction*, *IEEE Transactions on Medical Imaging* (2022).

[228] Green P. J., *Bayesian reconstructions from emission tomography data using a modified EM algorithm*, *IEEE Trans. Med. Imaging* **9** (1990) 84–93.

[229] De Pierro A. R., *A modified expectation maximization algorithm for penalized likelihood estimation in emission tomography*, *IEEE Trans. Med. Imaging* **14** (1995) 132–7.

[230] De Pierro A. R. and Yamagishi M. E. B., *Fast EM-like methods for maximum "a posteriori" estimates in emission tomography*, *IEEE Trans. Med. Imaging* **20** (2001) 280–8.

[231] Ahn S. and Fessler J. A., *Globally convergent image reconstruction for emission tomography using relaxed ordered subsets algorithms*, *IEEE Trans. Med. Imaging* **22** (2003) 613–26.

[232] Mumcuoglu E. Ü., Leahy R. M. and Cherry S. R., *Bayesian reconstruction of PET images: methodology and performance analysis*, *Phys. Med. Biol.* **41** (1996) 1777–807.

[233] Nuyts J., Beque D., Dupont P. and Mortelmans L., *A concave prior penalizing relative differences for maximum-a-posteriori reconstruction in emission tomography*, *IEEE Trans. Nucl. Sci.* **49** (2002) 56–60.

[234] Asma E., Ahn S., Ross S. G., Chen A. and Manjeshwar R. M., *Accurate and consistent lesion quantitation with clinically acceptable penalized likelihood images*, *2012 IEEE Nuclear Science Symposium and Medical Imaging Conference Record (NSS/MIC)* (2012) 4062–6.

[235] Ahn S., Ross S. G., Asma E., Miao J., Jin X., Cheng L., Wollenweber S. D. and Manjeshwar R. M., *Quantitative comparison of OSEM and penalized likelihood image reconstruction using relative difference penalties for clinical PET*, *Phys. Med. Biol.* **60** (2015) 5733–51.

[236] Alenius S. and Ruotsalainen U., *Bayesian image reconstruction for emission tomography based on median root prior*, *Eur. J. Nucl. Med. Mol. Imaging* **24** (1997) 258–65.

[237] Bettinardi V., Pagani E., Gilardi M., Alenius S., Thielemans K., Teras M. and Fazio F., *Implementation and evaluation of a 3D one-step late reconstruction algorithm for 3D positron emission tomography brain studies using median root prior*, *Eur. J. Nucl. Med. Mol. Imaging* **29** (2002) 7–18.

[238] Sidky E. Y. and Pan X., *Image reconstruction in circular cone-beam computed tomography by constrained, total-variation minimization*, *Phys. Med. Biol.* **53** (2008) 4777–807.

[239] Zhang Z., Ye J., Chen B., Perkins A. E., Rose S., Sidky E. Y., Kao C-M., Xia D., Tang C-H. and Pan X., *Investigation of optimization-based reconstruction with an image-total-variation constraint in PET*, *2015 IEEE Nuclear Science Symposium and Medical Imaging Conference (NSS/MIC)* (2015).

[240] Wang G. and Qi J., *Penalized Likelihood PET Image Reconstruction Using Patch-Based Edge-Preserving Regularization*, *IEEE Trans. Med. Imaging* **31** (2012) 2194–204.

[241] Ross S., *Q.Clear*, *GE Heal. White Pap.* (2014) .

[242] Teoh E. J., McGowan D. R., Macpherson R. E., Bradley K. M. and Gleeson F. V., *Phantom and Clinical Evaluation of the Bayesian Penalized Likelihood Reconstruction Algorithm Q.Clear on an LYSO PET/CT System*, *J. Nucl. Med.* **56** (2015) 1447–52.

[243] Ribeiro D., Hallett W., Howes O., McCutcheon R., Nour M. M. and Tavares A. A. S., *Assessing the impact of different penalty factors of the Bayesian reconstruction algorithm Q.Clear on in vivo low count kinetic analysis of [11C]PHNO brain PET-MR studies*, *EJNMMI Res.* **12** (2022) 11.

[244] Wang G. and Qi J., *PET Image Reconstruction Using Kernel Method*, *IEEE Trans. Med. Imaging* **34** (2015) 61–71.

[245] Cao S., He Y., Sun H., Wu H., Chen W. and Lu L., *Dynamic PET image reconstruction incorporating a median nonlocal means kernel method*, *Comput. Biol. Med.* **139** (2021) 104713.

[246] Ashouri Z., Wang G., Dansereau R. M. and DeKemp R. A., *Evaluation of Wavelet Kernel-based PET Image Reconstruction*, *IEEE Trans. Radiat. Plasma Med. Sci.* **6** (2022) 564-73.

[247] Deidda D., Karakatsanis N. A., Robson P. M., Tsai Y-J., Efthimiou N., Thielemans K., Fayad Z. A., Aykroyd R. G. and Tsoumpas C., *Hybrid PET-MR list-mode kernelized expectation maximization reconstruction*, *Inverse Probl.* **35** (2019) 044001.

[248] Mao X., Zhao S., Meng X., Jin Y., Kong H., Yuan J., He Q., Liang D., Yu J. and Hu Z., *PET parametric imaging based on MR frequency-domain texture information*, *Nucl. Instruments Methods Phys. Res. Sect. A Accel. Spectrometers, Detect. Assoc. Equip.* **1029** (2022) 166411.

[249] Barker W. C., Thada S. and Dieckmann W., *A GPU-accelerated implementation of the MOLAR PET reconstruction package*, *2009 IEEE Nuclear Science Symposium Conference Record* (2009) 4114–9.

[250] Herraiz J. L., España S., Cabido R., Montemayor A. S., Desco M., Vaquero J. J. and Udias J. M., *GPU-Based Fast Iterative Reconstruction of Fully 3-D PET Sinograms*, *IEEE Trans. Nucl. Sci.* **58** (2011) 2257–63.

[251] Galve P., Herraiz J. L., Catana C. and Udias J. M., *GPU based Fast and Flexible Iterative Reconstructions of Arbitrary and Complex PET Scanners: Application to Next Generation Dedicated Brain Scanners*, *2020 IEEE Nuclear Science Symposium and Medical Imaging Conference* (2020).

[252] Matsubara K., Ibaraki M., Nemoto M., Watabe H. and Kimura Y., *A review on AI in PET imaging*, *Ann. Nucl. Med.* **36** (2022) 133–43.

[253] Zhu B., Liu J. Z., Cauley S. F., Rosen B. R. and Rosen M. S., *Image reconstruction by domain-transform manifold learning*, *Nature* **555** (2018) 487–92.

[254] Häggström I., Schmidtlein C. R., Campanella G. and Fuchs T. J., *DeepPET: A deep encoder–decoder network for directly solving the PET image reconstruction inverse problem*, *Med. Image Anal.* **54** (2019) 253–62.

[255] Whiteley W., Luk W. K. and Gregor J., *DirectPET: full-size neural network PET reconstruction from sinogram data*, *J. Med. Imaging* **7** (2020) 1.

[256] Kandarpa V. S. S., Bousse A., Benoit D. and Visvikis D., *DUG-RECON: A Framework for Direct Image Reconstruction Using Convolutional Generative Networks*, *IEEE Trans. Radiat. Plasma Med. Sci.* **5** (2021) 44–53.

[257] Hu Z., Xue H., Zhang Q., Gao J., Zhang N., Zou S., Teng Y., Liu X., Yang Y., Liang D., Zhu X. and Zheng H., *DPIR-Net: Direct PET Image Reconstruction Based on the Wasserstein Generative Adversarial Network*, *IEEE Trans. Radiat. Plasma Med. Sci.* **5** (2021) 35-43.

[258] Wang B. and Liu H., *FBP-Net for direct reconstruction of dynamic PET images*, *Phys. Med. Biol.* **65** (2020) 235008.

[259] Zhang Q., Gao J., Ge Y., Zhang N., Yang Y., Liu X., Zheng H., Liang D. and Hu Z., *PET Image Reconstruction Using a Cascading Back-Projection Neural Network*, *IEEE J. Sel. Top. Signal Process.* **14** (2020) 1100-11.

[260] Feng T., Yao S., Xi C., Zhao Y., Wang R., Wu S., Li C. and Xu B., *Deep learning-based image reconstruction for TOF PET with DIRECT data partitioning format*, *Phys. Med. Biol.* **66** (2021) 165007.

[261] Ote K. and Hashimoto F., *Deep-learning-based fast TOF-PET image reconstruction using direction information*, *Radiol. Phys. Technol.* (2022) 0-23.

[262] Whiteley W., Panin V., Zhou C., Cabello J., Bharkhada D. and Gregor J., *FastPET: Near Real-Time Reconstruction of PET Histo-Image Data Using a Neural Network*, *IEEE Trans. Radiat. Plasma Med. Sci.* **1** (2021) 65–77.

[263] Yang B., Zhou L., Chen L., Lu L., Liu H. and Zhu W., *Cycle-consistent learning-based hybrid iterative reconstruction for whole-body PET imaging*, *Phys. Med. Biol.* **67** (2022) 085016.

[264] Gong K., Wu D., Li Q., Kim K., Yang J., El Fakhri G. and Seo Y., *EMnet: an unrolled deep neural network for PET image reconstruction Medical Imaging*, *2019: Physics of Medical Imaging ed H Bosmans, G-H Chen and T Gilat Schmidt (SPIE)* (2019) 185.

[265] Gong K., Wu D., Kim K., Yang J., Sun T., El Fakhri G., Seo Y. and Li Q., *MAPEM-Net: an unrolled neural network for Fully 3D PET image reconstruction*, *15th International Meeting on Fully Three-Dimensional Image Reconstruction in Radiology and Nuclear Medicine ed S Matej and S D Metzler (SPIE)* (2019) 102.

[266] Corda-D'Incan G., Schnabel J. A. and Reader A. J., *Iteration-Dependent Networks and Losses for Unrolled Deep Learned FBSEM PET Image Reconstruction*, *2020 IEEE Nuclear Science Symposium and Medical Imaging Conference (NSS/MIC) (IEEE)* (2020) 1–4.

[267] Corda-D'Incan G., Schnabel J. A. and Reader A. J., *Syn-Net for Synergistic Deep-Learned PET-MR Reconstruction*, *2020 IEEE Nuclear Science Symposium and Medical Imaging Conference (NSS/MIC) (IEEE)* (2020) 1–5.

[268] Xie Z., Baikejiang R., Li T., Zhang X., Gong K., Zhang M., Qi W., Asma E. and Qi J., *Generative adversarial network based regularized image reconstruction for PET*, *Phys. Med. Biol.* **65** (2020) 125016.

[269] Ulyanov D., Vedaldi A. and Lempitsky V., *Deep Image Prior*, *Int. J. Comput. Vis.* **28** (2020) 1867-88.

[270] Gong K., Catana C., Qi J. and Li Q., *PET Image Reconstruction Using Deep Image Prior*, *IEEE Trans. Med. Imaging* **38** (2019) 1655-65.

[271] Hashimoto F., Ote K. and Onishi Y., *PET Image Reconstruction Incorporating Deep Image Prior and a Forward Projection Model*, *IEEE Trans. Radiat. Plasma Med. Sci.* **7311** (2022) 1-1.

[272] Ote K., Hashimoto F., Onishi Y., Isobe T. and Ouchi Y., *List-Mode PET Image Reconstruction Using Deep Image Prior*, *IEEE Trans. Med. Imaging* (2022) http://arxiv.org/abs/2204.13404.

[273] Gong K., Guan J., Kim K., Zhang X., Yang J., Seo Y., El Fakhri G., Qi J. and Li Q., *Iterative PET Image Reconstruction Using Convolutional Neural Network Representation*, *IEEE Trans. Med. Imaging* **38** (2019) 675–85.

[274] Li S., Gong K., Badawi R. D., Kim E. J., Qi J. and Wang G., *Neural KEM: A Kernel Method with Deep Coefficient Prior for PET Image Reconstruction*, *IEEE Trans. Med. Imaging* (2022) http://arxiv.org/abs/2201.01443.

[275] Ouyang J., Chen K. T., Gong E., Pauly J. and Zaharchuk G., *Ultra-low-dose PET reconstruction using generative adversarial network with feature matching and task-specific perceptual loss*, *Med Phys* **46(8)** (2019) 3555-3564.

[276] Luo Y., Wang Y., Zu C., Zhan B., Wu X., Zhou J., Shen D. and Zhou L., *3D Transformer-GAN for High-Quality PET Reconstruction Medical Image Computing and Computer Assisted Intervention*, *MICCAI 2021 ed M de Bruijne, P C Cattin, S Cotin, N Padoy, S Speidel, Y Zheng and C Essert (Cham: Springer International Publishing)* (2021) 276-85.

[277] Zeng P., Zhou L., Zu C., Zeng X., Jiao Z., Wu X., Zhou J., Shen D. and Wang Y., *3D CVT-GAN: A 3D Convolutional Vision Transformer-GAN for PET Reconstruction*, *Medical Image Computing and Computer Assisted Intervention – MICCAI 2022. MICCAI 2022. Lecture Notes in Computer Science ed L Wang, Q Dou, P Fletcher, S Speidel and S Li* (2022) 516–26.

[278] Fei Y., Zu C., Jiao Z., Wu X., Zhou J., Shen D. and Wang Y., *Classification-Aided High-Quality PET Image Synthesis via Bidirectional Contrastive GAN with Shared Information Maximization*, *Medical Image Computing and Computer Assisted Intervention – MICCAI 2022. MICCAI 2022. Lecture Notes in Computer Science ed L Wang, Q Dou, P Fletcher, S Speidel and S Li* (2022) 527–37.

[279] Cui J., Xie Y., Joshi A. A., Gong K., Kim K., Son Y-D., Kim J-H., Leahy R., Liu H. and Li Q., *PET Denoising and Uncertainty Estimation Based on NVAE Model Using Quantile Regression Loss*, *Medical Image Computing and Computer Assisted Intervention – MICCAI 2022. MICCAI 2022. Lecture Notes in Computer Science ed L Wang, Q Dou, P Fletcher, S Speidel and S Li* (2022) 173–83.

[280] Liu Q., Liu H., Mirian N., Ren S., Viswanath V., Karp J., Surti S. and Liu C., *A personalized deep learning denoising strategy for low-count PET images*, *Phys. Med. Biol.* **67** (2022) 145014.

[281] Gambin J. R., Tadi M. J., Teuho J., Klen R., Knuuti J., Koskinen J., Saraste A. and Lehtonen E., *Learning to Denoise Gated Cardiac PET Images Using Convolutional Neural Networks*, *IEEE Access* **9** (2021) 145886–99.

[282] Cui J., Gong K., Guo N., Wu C., Meng X., Kim K., Zheng K., Wu Z., Fu L., Xu B., Zhu Z., Tian J., Liu H. and Li Q., *PET image denoising using unsupervised deep learning*, *Eur J Nucl Med Mol Imaging* **46(13)** (2019) 2780-2789.

[283] Chen K. T., Gong E., de Carvalho Macruz F. B., Xu J., Boumis A., Khalighi M., Poston K. L., Sha S. J., Greicius M. D., Mormino E., Pauly J. M., Srinivas S. and Zaharchuk G., *Ultra–low-dose 18F-florbetaben amyloid PET imaging using deep learning with multi-contrast MRI inputs*, *Radiology* **290(3)** (2019) 649-656.

[284] Cui J., Gong K., Guo N., Wu C., Kim K., Liu H. and Li Q., *Populational and individual information based PET image denoising using conditional unsupervised learning*, *Phys. Med. Biol.* **66** (2021) 155001.

[285] Schramm G., Rigie D., Vahle T., Rezaei A., Van Laere K., Shepherd T., Nuyts J. and Boada F., *Approximating anatomically-guided PET reconstruction in image space using a convolutional neural network*, *Neuroimage* **224** (2021) 117399.

[286] Herraiz J. L., Bembibre A. and López-Montes A., *Deep-Learning Based Positron Range Correction of PET Images*, *Appl. Sci.* **11** (2020) 266.

[287] Yang C-C., *Compensating Positron Range Effects of Ga-68 in Preclinical PET Imaging by Using Convolutional Neural Network: A Monte Carlo Simulation Study*, *Diagnostics* **11** (2021) 2275.

[288] Sanaat A., Akhavanalaf A., Shiri I., Salimi Y., Arabi H. and Zaidi H., *Deep-TOF-PET: Deep learning-guided generation of time-of-flight from non-TOF brain PET images in the image and projection domains*, *Hum. Brain Mapp.* **67** (2022) 145014.

[289] Hong X., Zan Y., Weng F., Tao W. and Peng Q., & Huang, Q., *Enhancing the image quality via transferred deep residual learning of coarse PET sinograms*, *IEEE Trans Med Imaging* **37(10)** (2018) 2322-2332.

[290] Shi J., Liu Q., Wang C., Zhang Q. and Ying, S., & Xu, H., *Super-resolution reconstruction of MR image with a novel residual learning network algorithm*, *Phys Med Biol* **63(8)** (2018) 085011.

[291] Song T. A., Chowdhury S. R., Yang F. and Dutta J., *PET image super-resolution using generative adversarial networks*, *Neural Networks* **125** (2020) 83-91.

[292] Sudarshan V. P., Egan G. F. and Chen Z., & Awate, S. P., *Joint PET-MRI image reconstruction using a patch-based joint-dictionary prior*, *Med Image Anal* **62** (2020) 101669.

[293] Malczewski K., *Super-Resolution with compressively sensed MR/PET signals at its input*, *Informatics in Medicine Unlocked* **18** (2020) 100302.

[294] Mehranian, A., & Reader, A. J. (2021). Model-based deep learning PET image reconstruction using forward-backward splitting expectation-maximization. IEEE Transactions on Radiation and Plasma Medical Sciences, 5(1), 54e64.